Akademia Górniczo-Hutnicza im. Stanisława Staszica w Krakowie
WYDZIAŁ FIZYKI I INFORMATYKI STOSOWANEJ

KATEDRA ODDZIAŁYWAŃ I DETEKCJI CZĄSTEK

Projekt dyplomowy

Investigation of rare processes with two photons in the final state in heavy-ion collisions at the LHC

Badanie rzadkich procesów z dwoma fotonami w stanie końcowym w zderzeniach ciężkich jonów na LHC

Autor: Kacper Zając
Kierunek studiów: Fizyka Techniczna
Opiekun pracy: prof. dr hab. inż. Iwona Grabowska-Bołd

Kraków, 2026

Acknowledgements

Research project partly supported by the program "Excellence Initiative - Research University" at the AGH University of Krakow, grant no. 15207.

I would really like to thank my supervisor, Iwona Grabowska-Bołd - Full Professor of Physics at the AGH University of Krakow and member of the ATLAS Collaboration - for her invaluable guidance and mentorship, not only throughout this research project but also beyond it. I am deeply grateful for the time she dedicated to helping me and for the opportunities she provided for my professional growth at this early stage of my scientific career. Her support was essential to this analysis and will undoubtedly remain so in the future.

I would also like to thank Adam Matyja - a Professor of IFJ PAN and member of the ALICE collaboration for helpful discussions and guidance in the preparation of the results presented in the section **Theoretical predictions for ALICE detector's phase space**. I am indebted to him for introducing me to the world of HEP analyses during my internship at the Institute of Nuclear Physics PAN. I am truly grateful for the opportunity to acquire the foundational knowledge and technical skills that I continue to apply and develop today.

It has been a true privilege to learn from such distinguished scientists, whose expertise and passion have shaped my path in physics.

If I have seen further, it is by standing on the shoulders of giants. - Isaac Newton

Table of Contents

1. Introduction

Monte Carlo (MC) simulations play a crucial role in modern particle physics, allowing the theoretical modelling and interpretation of complex collision processes studied at the Large Hadron Collider (LHC) at CERN. Many physics analyses would be difficult or impossible without MC generators, which provide model representations of particle interactions based on current knowledge and are essential for comparing theoretical predictions with experimental data. Besides their direct use in interpreting measured data in experiment, MC simulations assist in planning and optimizing detector and trigger configurations. In theory they can also perform feasibility studies of proposed measurements. They also play a key role in assessing background contributions and estimating both statistical and systematic uncertainties.

In this thesis various applications of MC generators are explored and utilized, ranging from their use in ongoing analyses, to performing feasibility studies that assess the theoretical significance of proposed, previously unexamined analyses. MC generators are applied specifically to ultra-peripheral Pb-Pb collisions at a centre-of-mass energy of $\sqrt{s_{\mathrm{NN}}} = 5.36$ TeV, corresponding to the Run 3 data-taking period at the LHC. The generators employed include SuperChic, UPCgen and MadGraph5. Each generator was employed to simulate specific photon- and gluon-induced processes relevant to the analyses. While MC simulations form the foundation of many studies presented in this thesis, this work also includes analysis based on real collision data of lead ions collected by the ATLAS experiment at the LHC during the 2025 data-taking period. In particular, trigger performance studies are discussed. This work is a result of the internship at CERN by Author who was assisting in heavy-ion data taking.

In the case of the ongoing ATLAS light-by-light analysis in Run 3, several rare photon-induced processes are investigated. In principle this includes light-by-light scattering ($\gamma\gamma \rightarrow \gamma\gamma$), CEP ($gg \rightarrow \gamma\gamma$), dipion production ($\gamma\gamma \rightarrow \pi^0\pi^0$) that has not been previously studied, and the $\gamma\gamma \rightarrow e^+e^-\gamma\gamma$ final state. Apart from its relevance to the ongoing ATLAS analysis, in the case of the ALICE experiment, the feasibility studies for the future (Run 3 and Run 4) are made. ALICE, like other detectors, continues to undergo significant upgrades, which will enable new measurements. In this context, feasibility studies of light-by-light scattering process with two proposed background contributions - dipion production and dielectron production ($\gamma\gamma \rightarrow e^+e^-$) - are made with the MC generators. Results of those studies may provide valuable input for the planning of future analyses within the ALICE physics program.

The results discussed in this thesis demonstrate the indispensable role of MC simulations in both the analyses and design of high-energy physics UPCs experiments complemented also by real data studies.

2. Theoretical background

2.1 Ultra-peripheral collisions

A heavy-ion collision can be classified as central, when the impact parameter b is smaller than the double radius of the colliding nuclei (ideally head-to-head), leading to a large overlap region and high particle multiplicity. It can also be peripheral, where the overlap between the colliding hadrons is partial and the strong interaction is reduced. Finally, there is an ultra-peripheral collision (UPC), in which the impact parameter is larger than the sum of the nuclei radii. In this case, the ions or protons from the incoming beam do not interact through the strong force but rather via the exchange of electromagnetic photon fluxes, allowing electromagnetic or photo-nuclear processes to occur while the projectiles remain intact after the interaction. Figure 2.1 schematically illustrates the difference between central and UPCs.

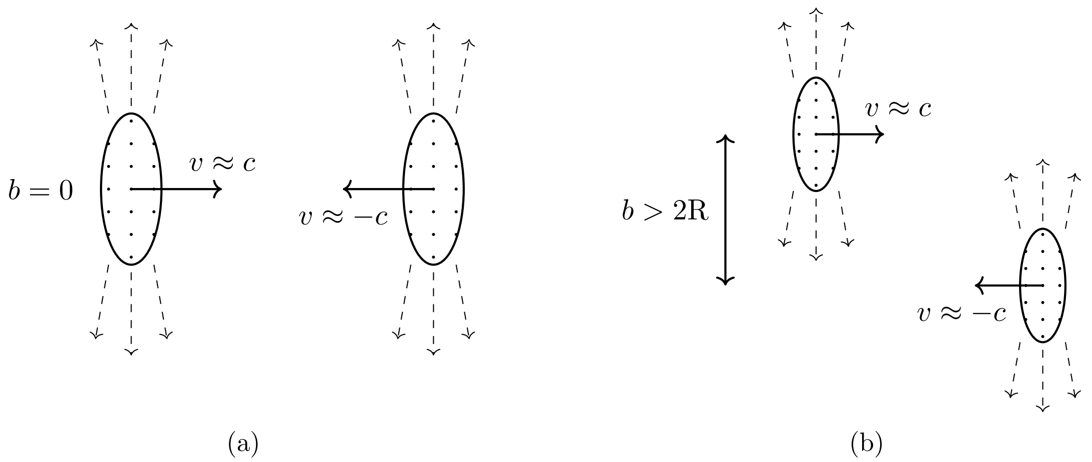

Figure 2.1: Scheme of ultra-relativistic (a) central collision with $b = 0$ and (b) ultra-peripheral collision with $b > 2\mathrm{R}$, where R represents a radius of each ion. Dashed arrows represents flux of photons (electromagnetic field of the ion).

Each fast-moving charged ion generates a strong electromagnetic field, which in the relativistic limit can be described as a flux of quasi-real photons. These photons can interact with one another ($\gamma\gamma$ interactions) or with the other nucleus (γA interactions), leading to a variety of photon-induced processes. The Equivalent Photon Approximation (EPA), also known as the Weizsäcker-Williams method, provides a convenient way to describe such interactions [1]. It replaces the time-varying electromagnetic field of a relativistic charged particle with an equivalent flux of photons characterized by an energy spectrum depending on Z and Lorentz factor γ. This approach allows the use of standard photon-photon and photon-hadron cross sections in the calculation of UPC event rates. In addition, since the interacting ions remain intact and no strong interaction occurs, UPC events exhibit a very clean experimental signature with low multiplicity and minimal background. This makes them an excellent testing ground for both quantum electrodynamics (QED) and quantum chromodynamics (QCD) photon-induced processes at high energies.
In the case of UPCs, MC generators may differ due to the use of various photon flux models, leading to variations in the predicted final states. These differences stem from distinct assumptions regarding the electromagnetic fields of the nuclei, the impact param-

eter dependence, and the treatment of photon virtuality. As a result, each generator can produce slightly different predictions for cross sections, kinematic distributions, and event topologies for the same elementary physical process.

2.2 Light-by-light scattering

Light-by-light (LbyL) scattering is a very rare process in which two photons interact with each other via a one-loop box diagram, resulting in the production of two photons in the final state ($\gamma\gamma \rightarrow \gamma\gamma$). In other words, a pair of photons scatter off one another - a phenomenon forbidden in classical electrodynamics but predicted in 1936 within the framework of QED [2]. The left panel of Figure 2.2 shows the Feynman diagram for the LbyL scattering process, mediated by a virtual one-loop box. The particles mediating inside the loop carry electric charge, and they can be either fermions (such as leptons or quarks) or $W^{\pm}$ bosons. Since the diagram involves four electromagnetic vertices, each proportional to the fine-structure constant α_{em}, the leading-order cross section is proportional to $\alpha_{\text{em}}^4 \approx 3 \times 10^{-9}$ [3]. This extremely small coupling makes the process many orders of magnitude rarer than typical QED or QCD interactions.

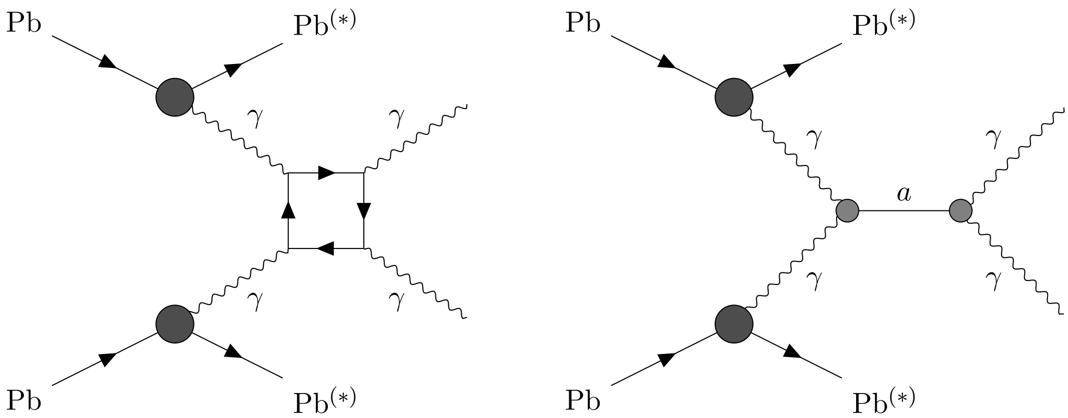

Figure 2.2: Feynman diagrams of LbyL in Pb-Pb UPCs. On the left Standard Model description with one-loop box, on the right axion-like (a) narrow resonance. Possible electromagnetic excitation of the outgoing Pb ions is denoted by ($*$).

To enhance the probability of observing such a rare process, LbyL scattering is studied in UPCs of heavy ions, such as lead (Pb-Pb) - which was described in Section 2.1. UPCs provide an ideal environment for this measurement because strong interactions are suppressed; the process is dominated by electromagnetic interactions. Moreover, the photon flux associated with a relativistic ion is proportional to the square of its charge (Z^2) as described with the Weizsäcker-Williams formula, which significantly increases the effective cross section in case of Pb beams and enhances the detectability of rare processes such as LbyL scattering.
In order to measure LbyL scattering, one searches for two photons in the final state where an interaction occurred between two heavy ions that remained intact. Only two energy deposits from the photons are expected in the electromagnetic calorimeter, with no associated tracks reconstructed in the tracking detectors. Since the LbyL process is extremely rare, even in Pb-Pb collisions, the number of collected events is small due to the limited integrated luminosity achievable at the LHC.

For example the first direct observation of LbyL scattering in history was reported by the ATLAS in 2017 [4]. Two years later, in 2019 CMS also documented its evidence [5]. Using data recorded in 2015 at centre of mass energy of $\sqrt{s_{\text{NN}}} = 5.02$ TeV per nucleon-pair, the experiments provided evidence for the process. In ATLAS a total of 13 candidate events were observed, with a background of 2.6 ± 0.7 events. This result represented the first direct experimental confirmation of photon-photon scattering, observed with a significance of 4.2 standard deviations, providing a clear and compelling indication of the process. Measured cross section for the process of about 70 ± 24 (stat.) $\pm$ 17 (syst.) nb, was in agreement with the predictions, however as one can see the statistics were really low, therefore the cross section measured by the experiment has high uncertainty. An updated measurement was then performed, as reported in Ref. [6], combining Pb-Pb collision data recorded by ATLAS in 2015 and 2018, for a total integrated luminosity of 2.2 nb^{-1}, but still with low statistics. This provides a strong motivation for further studies of this rare process using larger datasets collected in subsequent LHC runs, in order to improve the measurement precision and verify its consistency with the Standard Model.
Moreover, LbyL scattering is sensitive to potential contributions from physics beyond the Standard Model (BSM). For example, neutral axion-like particles (ALPs) could manifest as a narrow diphoton resonance, leading to modifications in the measured cross section, as illustrated in the right panel of Figure 2.2. ALPs are appearing in many theories involving spontaneously broken global symmetries. Their predicted masses and couplings to Standard Model particles span a wide range, making the diphoton final state an excellent channel to search for them. Previous ATLAS searches for ALPs decaying into photons have primarily been conducted in proton-proton [7, 8] and Pb-Pb [6] collisions data.
Other new-physics scenarios, such as those involving exotic charged particles or additional spatial dimensions, could also affect this process. Therefore, as LbyL scattering is a sensitive channel to new physics, collecting more data and performing increasingly precise measurements of LbyL scattering remain essential to probe possible deviations from Standard Model predictions.

2.3 Central exclusive production

Central Exclusive Production (CEP) is a process where the incoming protons or ions remain intact, and all produced particles appear in the central system. Because of that, such interaction has to be t-channel exchange of a colour-singlet object (like a photon or a gluon pair in a singlet state) [9]. Energy and momentum can be transferred without destroying the initial particles, preserving the exclusive nature of the event. If the interaction occurred through an s-channel with a coloured intermediate state, the strong interaction would break the protons or ions.
One way this can occur is through photon-photon fusion ($\gamma\gamma \rightarrow X$), where the photons originate from the electromagnetic fields of the passing charged particles. This particle-like description of the electromagnetic field is formalized using EPA. This approach simplifies calculations for photon-mediated processes by replacing the particle's electromagnetic field with a flux of quasi-real photons, allowing one to exploit the well-known properties of photons in the simulation. Alternatively, such a process can be mediated only strongly, so with gluons (pomerons, as it requires a color-singlet exchange) instead of photons or also can be mixed when one proton (ion) would interact electromagnetically and the second one strongly.

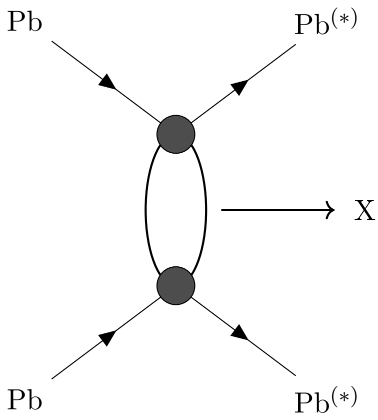

Figure 2.3: Central Exclusive Production scheme in Pb-Pb UPC where final state X is produced. Elipsoid represents an effective interaction.

In the context of LbyL scattering analyses, CEP background we are thinking of is diphoton production induced by gluons (pomeron-pomeron fusion) which is shown in Figure 2.4. CEP processes can be either coherent, where both nuclei remain intact after the interaction leading to very low transverse momentum of the final state system, or incoherent, where one or both nuclei dissociate. Although the kinematics of CEP events typically differ from pure photon-induced LbyL scattering - for example in transverse momentum distributions and photon rapidities - these processes can mimic the signal if not properly suppressed or modelled. MC simulations of CEP processes are therefore essential to estimate the expected background contribution. This allows one to optimize event selection criteria, such as cuts on photon transverse momentum, acoplanarity, or the absence of additional particles, to enhance the sensitivity to genuine LbyL events while minimizing contamination from CEP.

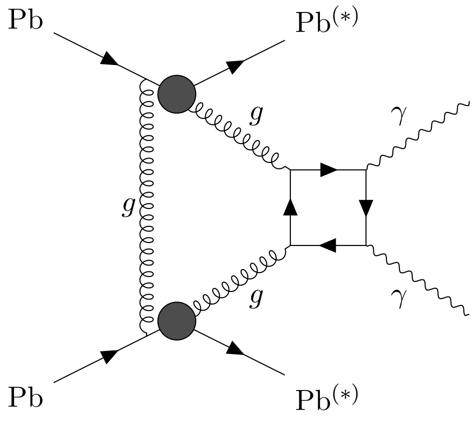

Figure 2.4: Feynman diagram of gluon-induced diphoton production ($gg \to \gamma\gamma$) in Pb-Pb UPCs.

2.4 Other processes

In the investigation of LbyL scattering, the dominant background process is the exclusive electron-positron pair production ($\gamma\gamma \to e^+e^-$), in which the $e^\pm$ can be misidentified as photons in the detector or if electrons undergo hard bremsstrahlung emitting high-energetic photons. The production of such charged particle pairs is more significant compared to the LbyL signal, as the corresponding Feynman diagram involves fewer vertices (two instead of four), as shown in Figure 2.5.

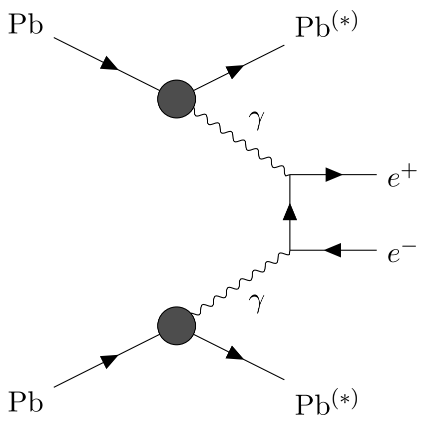

Figure 2.5: Feynman diagram of electron-positron pair production ($\gamma\gamma \to e^+e^-$) in Pb-Pb UPCs.

Moreover, electron-positron pair production is not the only possible background of this kind. A similar diagram can be drawn by replacing the $e^{\pm}$ with neutral pions (π^0), as illustrated in Figure 2.6.

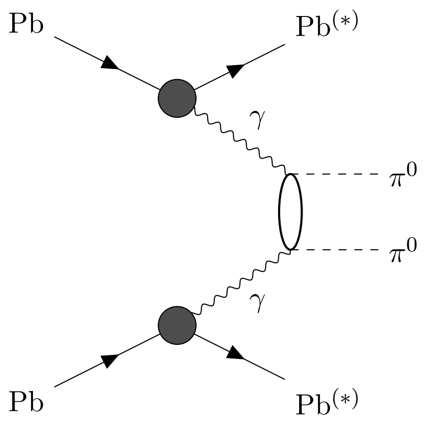

Figure 2.6: Feynman diagram of dipion production ($\gamma\gamma \to \pi^0\pi^0$) in Pb-Pb UPCs. Elipsoid represents an effective interaction.

This process ($\gamma\gamma \to \pi^0\pi^0$) has been proposed as an additional potential background contribution at lower energies, as discussed in Ref. [10]. Neutral pions primarily decay into two photons, so in the final state where dipion production occurred, a total of four photons is expected ($\pi^0\pi^0 \to (\gamma\gamma)(\gamma\gamma)$). Such a process can mimic LbyL diphoton signal if two out of the four photons are outside the detector's acceptance, or if the pairs of photons from the same pion are misidentified as a single photon with higher energy. In this process, two neutral pions are produced in a quasi-exclusive electromagnetic interaction, and each of them decays as:

$$\pi^0 \to \gamma\gamma.$$

Each photon pair originating from the same pion has an invariant mass of [11]:

$$m_{\gamma\gamma} \simeq m_{\pi^0} \approx 135 \text{ MeV},$$

and the two photons are emitted with a small opening angle in the laboratory frame. Such photon pairs exhibit strong kinematic correlations and populate a narrow invariant-mass range at m_{π^0}. They can be easily identified as π^0 candidates and thus do not represent a realistic background for LbyL scattering. However if photon pairs would be composed of photons originating from different pions (one photon from each π^0 decay) their invariant mass would constrain the pion mass. So if such situation would occur finally leading to a diphoton final state, such a process could become a significant background for the LbyL signal.

Other possible processes affecting the measurement of LbyL scattering include the production of various resonances that decay into photon pairs, such as η, or η' mesons. These resonances can mimic the LbyL signal if their decay photons are reconstructed as originating from an exclusive electromagnetic interaction, particularly in events with low transverse momentum and no additional activity in the detector.

3. Apparatus

3.1 Monte Carlo methods in High-Energy Physics

MC methods are powerful computational techniques that use randomly generated numbers to solve complex mathematical, statistical, or physical problems that are difficult to tackle with standard algorithms. The main concept of MC methods is to employ randomness to simulate inherently probabilistic processes, such as those encountered in quantum physics. Their name originates from the 'Monte Carlo' casino in Monaco, as mathematician Stanisław Ulam was inspired by his uncle's gambling habits when naming them [12].

In high-energy physics, the processes analyzed using data from the Large Hadron Collider are often too complex to be described analytically. This is where MC methods are particularly useful, providing a practical way to simulate events resulting from particle collisions. MC event generators encode our theoretical knowledge of fundamental interactions - especially QED, QCD, and weak interactions into software tools capable of generating realistic predictions for experiments performed at colliders. As quantum mechanics is fundamentally probabilistic, MC event generators can use (pseudo)random numbers to reproduce different possible outcomes according to quantum-mechanical probabilities.

The event generation process in a typical MC generator consists of several stages. It begins with the simulation of the hard scattering, which is the primary interaction between partons (quarks or gluons) inside the colliding hadrons. The probability of producing a particular final-state particle or set of particles is determined by the matrix element of such a process, which encodes the quantum-mechanical amplitudes calculated from the underlying theory (above-mentioned QED, QCD, or weak interactions). The matrix element defines the relative likelihood of each possible outcome, and the generator uses random sampling to select events according to these probabilities. However, before the hard scattering, initial-state radiation (ISR) is simulated. ISR occurs because colliding particles are accelerated and carry non-zero colour charges (and often also electromagnetic charges). In this context, bremsstrahlung manifests as the emission of photons or gluons from the incoming particles. As a result, the momenta and other quantum numbers (degrees of freedom) of the hadrons can be modified prior to the collision. After the hard scattering, outgoing particles can also emit similar radiation, known as final-state radiation (FSR). The description above applies to a single pair of nucleons, but in collisions of heavier ions (such as Pb-Pb), multiple parton pairs can interact, leading to further ISR and FSR within these additional interactions.

Each colliding parton carries a fraction of the momentum of its parent hadron, and these fractions are described by the Parton Distribution Functions (PDF). PDFs are a critical ingredient in the simulation, as they provide the probability of finding a parton with a given momentum fraction inside the hadron [13]. Different PDF sets, obtained from global fits to experimental data, influence predicted cross sections and kinematic distributions. Careful consideration of PDF uncertainties is necessary, since they propagate directly to predictions of experimental observables. Partons which could be produced and radiated after collision cannot exist freely due to colour confinement [13]. The generator simulates then the hadronisation process by which partons combine into colour-neutral hadrons, such as mesons and baryons. Popular models include the Lund string model and cluster hadronisation, which employ probabilistic rules consistent with QCD phenomenology [14]. Unstable hadrons subsequently decay according to known branching ratios and lifetimes, producing the final-state particles that can be detected in experiments. After these steps

(and several more detailed procedures), a single event is generated, providing "truth-level" information about the underlying process. In reality, however, detector effects and limitations must be taken into account. Therefore, these truth events are passed through the detector simulation such as GEANT4 [15] to produce realistic predictions of detector signals and to test analysis strategies before real data is collected.
Accurate simulations are essential for many analyses, as they allow physicists to model both the expected signal and the background processes. By producing detailed final-state information for each simulated event, MC generators enable the prediction of virtually any observable or combination of observables, which can then be directly compared with experimental measurements. Furthermore, MC generators play a critical role in searches for new physics. They help quantify how unusual or significant a potential signal is, giving researchers confidence in their interpretation of excesses, evidences or new discoveries. Beyond immediate analyses, generators assist theorists and experimentalists in planning future experiments, estimating event rates, testing detector responses, helping design them, and optimizing experimental configurations before any data is collected. Theorists can also perform feasibility studies of specific physics processes and assess their potential significance.

3.2 Monte Carlo generators in UPC

3.2.1 SuperChic

SuperChic [16] is a Fortran-based MC event generator developed for the simulation of exclusive and photon-initiated processes in proton-proton and heavy-ion collisions. It includes a realistic treatment of the EPA, with configurable photon fluxes that account for proton and nuclear form factors, as well as coherent and incoherent photon emission. This makes SuperChic particularly suitable for studies of photon-initiated reactions in UPC heavy-ion collisions, where the electromagnetic fields of the ions dominate the interaction. SuperChic provides precise predictions for Standard Model final states at parton level and is widely used to simulate photon and gluon-initiated processes such as:

- LbyL scattering ($\gamma\gamma \to \gamma\gamma$),
- dilepton production ($\gamma\gamma \to l^+l^-$),
- CEP, including gluon-induced diphoton production ($gg \to \gamma\gamma$),
- production of hypothetical exclusive resonances, axion-like particles, and other rare signatures.

The generator offers a broad set of configurable parameters, including:

- coherent vs. incoherent emission switches,
- nuclear-breakup modelling, with the option to generate neutron emission in the forward direction,
- PDF set selection for nucleon and nuclear gluon distributions,
- kinematic cuts at generator level (transverse momentum, pseudorapidity, invariant mass etc.),
- centre-of-mass energy and more.

These features allow SuperChic to model realistic aspects of UPC dynamics, making it also directly applicable to analyses of neutron-emission topologies and exclusive final states. SuperChic has been extensively validated and is used by major LHC experiments: ATLAS, CMS, LHCb, and ALICE for theoretical studies, MC predictions, and background estimation in analyses involving exclusive and photon-induced processes in both proton-proton and heavy-ion UPC collisions.

In this analysis, SuperChic is configured for Pb-Pb UPCs at the LHC energies and phase spaces. The generator is used to obtain differential and total cross sections for LbyL scattering, exclusive dielectron production, CEP diphoton production, and other photon-induced processes relevant for signal and background modelling. For incoherent gluon-induced exclusive process CEP, several proton and nuclear PDF sets are tested to assess the impact of parton-density uncertainties on the predicted CEP yields.

3.2.2 UPCgen

UPCgen is a MC generator developed in C++, specifically for UPC heavy-ion collisions, introduced in Ref. [17]. Its purpose is to provide an improved and fully differential description of photon-photon interactions in nuclear environments. The generator constructs the $\gamma\gamma$ luminosity by folding the nuclear photon flux with the elementary subprocess cross section at the level of differential distributions, allowing for a more precise treatment than factorised or approximate schemes. As the authors of the generator say, UPCgen employs realistic nuclear form factors and permits photon emission from the full nuclear charge distribution, which affects both the shape and normalisation of the effective $\gamma\gamma$ spectrum. Photon polarisation effects are included explicitly, and the code allows variations of lepton anomalous magnetic moments, making it suitable for studies of dilepton final states within and beyond the Standard Model. In comparison to SuperChic, UPCgen focuses exclusively on two-photon induced processes and does not incorporate gluon-initiated exclusive production. The main differences between the generators arise from their handling of the photon flux, the coherence conditions, and the construction of the $\gamma\gamma$ luminosity.

In this analysis, UPCgen was used to obtain predictions for the process that is available in both generators (SuperChic and UPCgen): LbyL scattering ($\gamma\gamma \to \gamma\gamma$), enabling a comparison of their modelling approaches. An important advantage of UPCgen is the fact of its direct support for exclusive dipion production ($\gamma\gamma \to \pi^0\pi^0$), which is not implemented in any other UPC generator and is particularly relevant for studying lower invariant mass regions where this process can be a potential background for LbyL scattering.

3.2.3 MadGraph5

MC event generation can be performed using the MadGraph5 framework, a modern and versatile tool widely used for simulating high-energy particle collisions. MadGraph5 provides precise matrix-element calculations for a broad range of processes within and beyond the Standard Model, allowing flexible specification of complex initial and final states. It is commonly used to produce parton-level events, which can then be interfaced with parton showering, hadronisation (typically using PYTHIA), and detector simulation. Its modular structure and high level of automation make it well suited for studies requiring accurate kinematic modelling and reliable event generation.

In this analysis, MadGraph5 is employed to generate photon-induced interactions in UPC Pb-Pb collisions, providing simulated samples for the $\gamma\gamma \to e^+e^-\gamma\gamma$ process. This approach allows for an accurate description of the kinematic properties of exclusive dilepton events, including effects from final-state radiation (FSR).

3.3 Large Hadron Collider

The Large Hadron Collider (LHC) is the world's largest and most powerful particle accelerator, currently achieving collision energies up to 13.6 TeV in proton-proton collisions during its current operations. For heavy-ion collisions, such as lead-lead, the LHC has reached center-of-mass energies of about 5.36 TeV per nucleon pair. Among the many experiments operating at the LHC, the four main ones are ATLAS, CMS, ALICE and LHCb. The LHC was designed to probe the deepest structure of matter, test the Standard Model, search for new physics and study strongly interacting matter under extreme conditions. It began operating in 2008 and has since achieved several landmark results, including the discovery of the Higgs boson, the observation and characterization of quark-gluon plasma in heavy-ion collisions, studies of numerous hadronic resonances, as well as the observation of LbyL scattering. To reach such results, especially to observe extremely rare processes, experiments require very large datasets, meaning high integrated luminosity. These data are collected in operational periods known as Runs. The LHC first delivered collisions during Run 1 (2010-2013) at center-of-mass energies of 7-8 TeV for proton-proton collisions, allowing the initial discoveries, including the Higgs boson. After upgrades during Long Shutdown 1 (2013-2015), Run 2 (2015-2018) took place at 13 TeV, providing higher collision rates and enabling more precise measurements of rare processes and heavy particles. As of the end of 2025, the LHC is still operating in Run 3 (2022-2026), which is scheduled to continue until the end of June 2026. After this period, the accelerator will enter Long Shutdown 3 (LS3), lasting approximately 47 months. This technical shutdown will allow major upgrades to both the accelerator and the experiments in preparation for the next phase. Once LS3 is complete, the era of the High-Luminosity LHC will begin, during which significantly higher luminosity will be delivered, enabling unprecedented precision and access to even rarer phenomena.

In order to describe the kinematics of particles produced at the LHC, a standard detector coordinate system is used [18]. Cylindrical coordinates (r, ϕ) are defined in the plane transverse to the beam direction (z axis), with ϕ denoting the azimuthal angle around the z axis. The polar angle with respect to the z axis is denoted by θ. The transverse momentum p_{T} is defined as the component of the particle momentum perpendicular to the beam axis. The pseudorapidity η is defined in terms of the polar angle θ as:

$$\eta = -\ln\left[\tan\left(\frac{\theta}{2}\right)\right]. \tag{3.1}$$

It provides a convenient measure of the particle direction along the beam axis and is particularly useful because differences in pseudorapidity are invariant under Lorentz boosts along the beam direction. Where relevant, the rapidity:

$$y = \frac{1}{2}\ln\left(\frac{E + p_z c}{E - p_z c}\right), \tag{3.2}$$

is used to characterize the longitudinal kinematics. In the ultra-relativistic limit, and in particular for massless particles such as photons, the rapidity coincides with the pseudorapidity, $y \simeq \eta$.

In this work, the focus will be placed on the ATLAS experiment - in particular on its ongoing Run 3 analysis of LbyL scattering as well as on ALICE, specifically on the region of its phase space for which a feasibility study of LbyL measurements has been performed.

4. Light-by-light scattering in ATLAS

4.1 Light-by-light MC predictions

LbyL scattering ($\gamma\gamma \to \gamma\gamma$) can be observed in UPCs of heavy ions, where the electromagnetic fields of charged particles can be described using the EPA. This environment is ideal for studying rare photon-initiated processes. When LbyL scattering occurs, the final-state photons are produced back-to-back. MC samples are produced with 50 000 events for each generator for Pb-Pb collisions at the centre of mass energy of 5.36 TeV and fiducial requirements for final state photons: $p_{\mathrm{T}} > 2$ GeV, $m_{\gamma\gamma} > 4$ GeV and $|\eta| < 2.5$. Integrated fiducial cross sections are: 137.77 ± 0.07 nb and 128 nb for SuperChic 4.2 and UPCgen, respectively. After generating events, additional cut on $|\eta| < 2.4$ was made. To better understand the properties of the LbyL final state, Figures 4.1-4.5 present several key control distributions for the process under consideration in addition for two different MC generators: SuperChic 4.2 and UPCgen, along with their ratios. In addition two plots of different variables are shown in Appendix - Figure A.1. Distributions are normalised to 1 in order to compare their shapes. Below both the fundamental theoretical features of the signal and the differences between the generators are discussed.

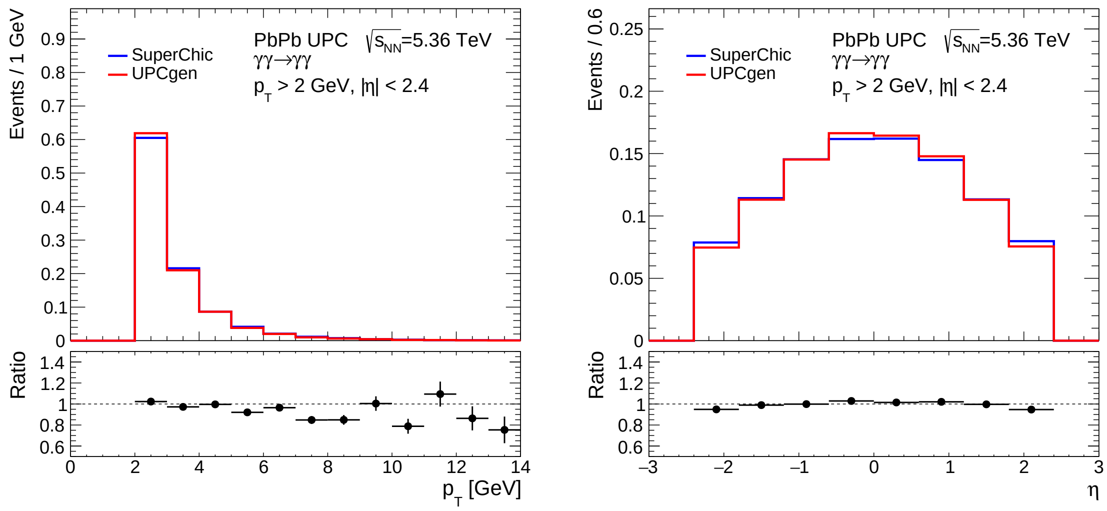

Figure 4.1: Transverse momentum p_{T} (left) and pseudorapidity η (right) normalised distributions of final-state photons from LbyL scattering ($\gamma\gamma \to \gamma\gamma$) coming from SuperChic 4.2 and UPCgen MC generators. Lower panel shows ratio of the two distributions, with error bars representing the statistical uncertainties on the ratio.

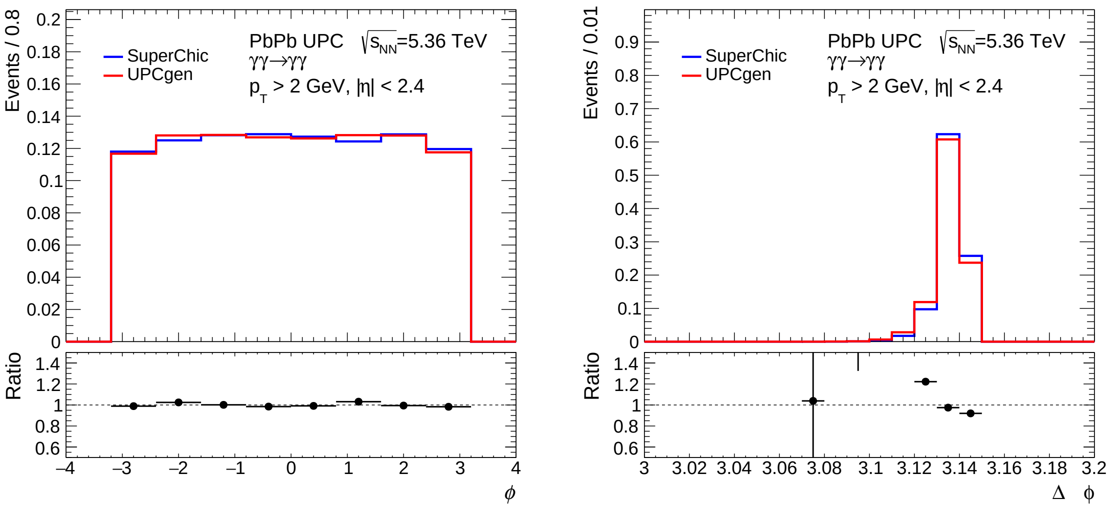

Figure 4.2: Azimuthal angle ϕ (left) and difference in it between particles $\Delta\phi$ (right) normalized distributions of final state photons from LbyL scattering ($\gamma\gamma \to \gamma\gamma$) coming from SuperChic 4.2 and UPCgen MC generators.

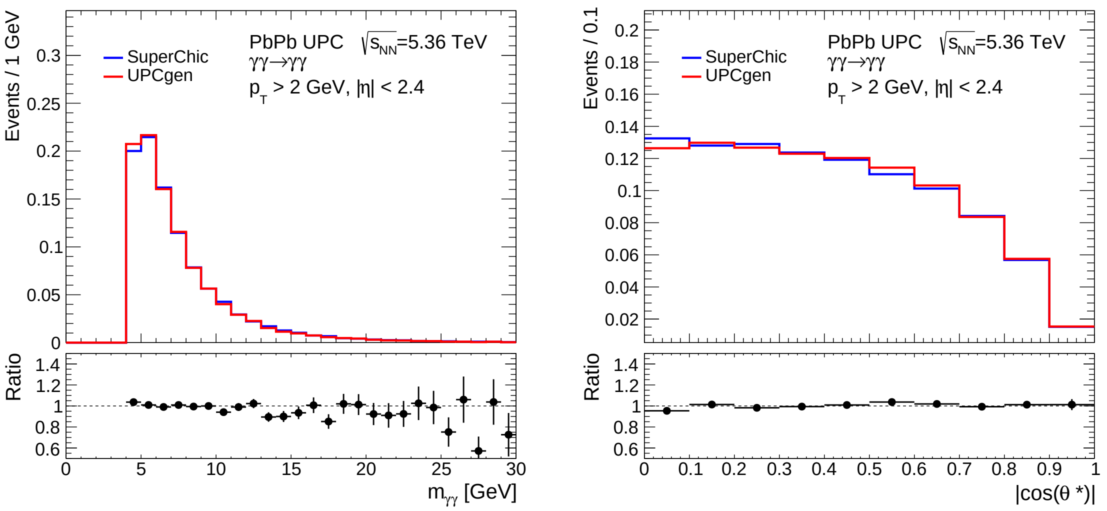

Figure 4.3: Diphoton invariant mass $m_{\gamma\gamma}$ (left) and $\cos(\theta^*)$ (right) normalized distributions of final state photons from LbyL scattering ($\gamma\gamma \to \gamma\gamma$) coming from SuperChic 4.2 and UPCgen MC generators.

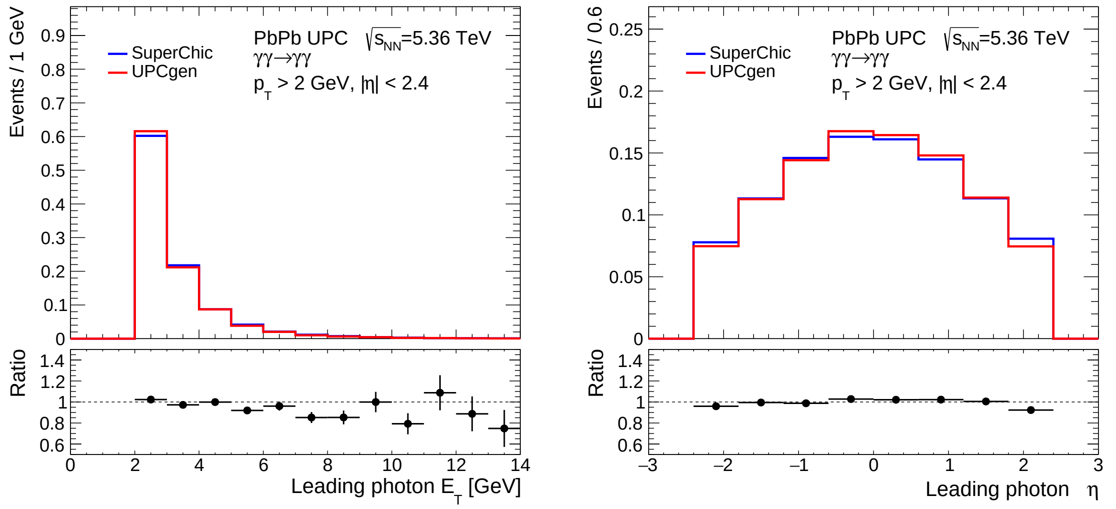

Figure 4.4: Leading photon transverse momentum p_T (left) and pseudorapidity η (right) normalized distributions of final state photons from LbyL scattering ($\gamma\gamma \to \gamma\gamma$) coming from SuperChic 4.2 and UPCgen MC generators.

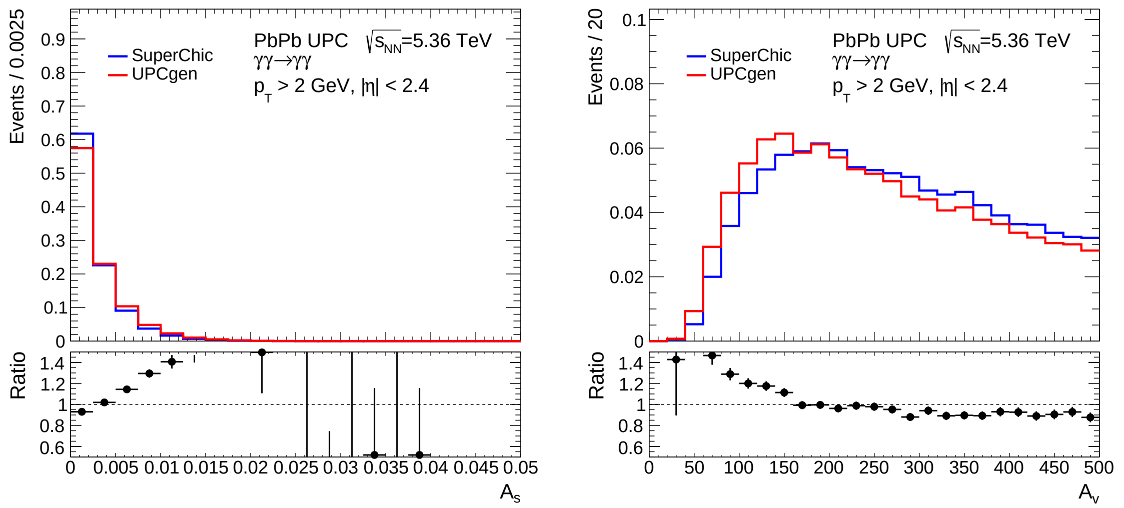

Figure 4.5: Scalar asymmetry A_S (left) and vector asymmetry A_v (right) normalized distributions of final state photons from LbyL scattering ($\gamma\gamma \to \gamma\gamma$) coming from SuperChic 4.2 and UPCgen MC generators.

In Figure 4.1 the distributions of the transverse momentum p_T and pseudorapidity η of the outgoing final-state photons from LbyL are shown. The p_T distribution starts at 2 GeV, while the pseudorapidity satisfies $|\eta| < 2.4$, as defined in the setup of both generators. Both generators predict similar shapes for these variables; however, in the case of transverse momentum, small differences can be observed in a few bins around 5-6 GeV and 7-9 GeV. Differences at higher p_T values are less conclusive due to limited statistics in the high-p_T region. The angular distributions from Figure 4.2 are very similar for both generators. As seen in the $\Delta\phi$ distributions, photons are mostly produced back-to-back, with a peak near π (180°). Nonetheless, differences appear in some bins, especially with lower statistics. A similar behaviour is expected for the acoplanarity distribution, defined as:

$$\text{Aco} = 1 - \frac{\Delta\phi}{\pi}. \tag{4.1}$$

In the case of the invariant mass distribution shown in the left panel of Figure 4.3, one observes a trend analogous to the transverse momentum distributions but overall the predictions from both generators agree in shapes over the entire spectrum. Variable visible on the right-hand side of Figure 4.3 $|\cos(\theta^*)|$ is defined as:

$$|\cos(\theta^*)| = \left|\tanh\left(\frac{\Delta y_{\gamma1,\gamma2}}{2}\right)\right|, \tag{4.2}$$

where θ^* is the diphoton scattering angle in the diphoton centre-of-mass frame and $\Delta y_{\gamma1,\gamma2}$ is difference between rapidities of both photons. Distributions of it are also consistent between the generators. Figure 4.4 presents the p_{T} and η distributions for the leading photon; the conclusions remain the same as for the distributions of both final-state photons. Finally, the distributions shown in Figure 4.5 correspond to more "exotic" observables, namely the scalar and vector asymmetries proposed in Ref. [19]. The scalar asymmetry A_{S} is a relative difference in transverse momentum of two final-state particles and for the back-to-back photons it peaks at 0, it is defined as:

$$A_{\mathrm{S}} = \left|\frac{|\vec{p}_{\mathrm{T},\gamma1}| - |\vec{p}_{\mathrm{T},\gamma2}|}{|\vec{p}_{\mathrm{T},\gamma1}| + |\vec{p}_{\mathrm{T},\gamma2}|}\right|. \tag{4.3}$$

The vector asymmetry A_{v} in contrast distribute at high values for back-to-back particles due to defined denominator:

$$A_{\mathrm{v}} = \frac{|\vec{p}_{\mathrm{T},\gamma1} + \vec{p}_{\mathrm{T},\gamma2}|}{|\vec{p}_{\mathrm{T},\gamma1} - \vec{p}_{\mathrm{T},\gamma2}|}. \tag{4.4}$$

For both asymmetries, larger differences between the generators are observed. For the scalar asymmetry, the discrepancies may be attributed to limited statistics, whereas for the vector asymmetry, significant differences appear, particularly in the region of $A_{\mathrm{v}} < 150$. Overall, despite minor differences in specific bins and low-statistics regions, the predictions from both generators are remarkably consistent. Across most observables, they produce very similar distributions, indicating that the overall modelling of LbyL scattering in both SuperChic 4.2 and UPCgen for the phase space defined by the ATLAS detector is in good agreement. Having established the signal control distributions predicted by the MC generators, now one can proceed with further investigations of this rare process.

4.1.1 Dependence on collision energy

Since its construction, the LHC has been continuously developing; for example, it increased its centre-of-mass energy for Pb-Pb collisions, reaching a value of 5.36 TeV per nucleon pair in November 2022 at the start of Run 3. As energy rises, the cross sections also get higher, making it possible to register more events for the process of interest for the same value of integrated luminosity. However, the energy not only has impact on the cross section but also may change shapes of various kinematic variables. In this section it is evaluated if changing the collision energy has impact on the various kinematic distributions in the case of LbyL scattering. In order to check that, LbyL scattering MC samples were generated in two different UPC MC generators: SuperChic and UPCgen. Figures 4.6-4.7, together with additional distributions shown in Appendix A.2 present comparisons of different kinematic variables for energies of 5.02 TeV (Run 2) and 5.36 TeV (Run 3) obtained from the SuperChic 4.2 generator for LbyL scattering ($\gamma\gamma \to \gamma\gamma$). Distributions are normalised to unity in order to check only their shapes, because it is expected that at higher collision energy the number of events would just simply increase.

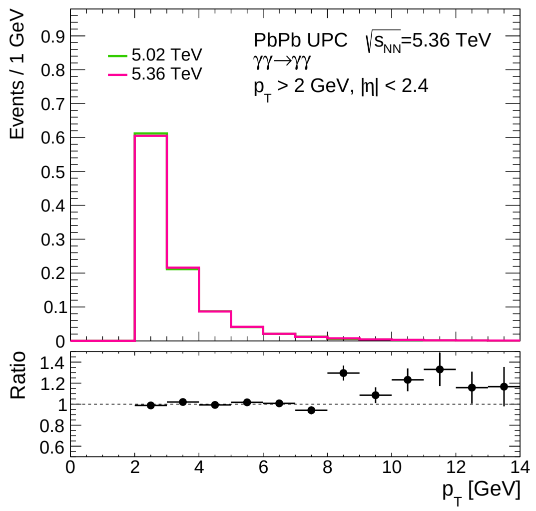

Figure 4.6: Comparison of photon $p_{\rm T}$ (left) and pseudorapidity η (right) of distributions obtained for different collision energies coming from SuperChic 4.2.

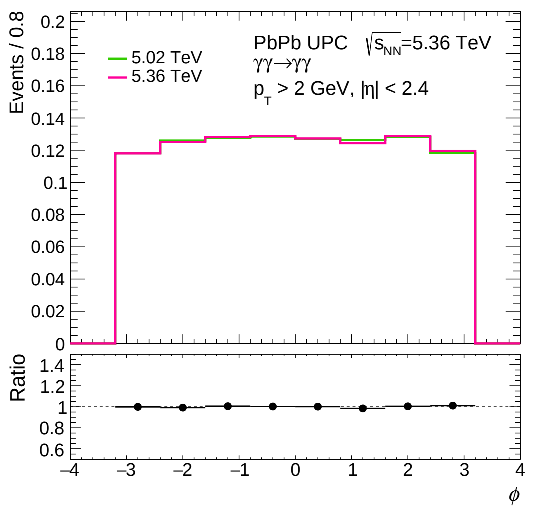

Figure 4.7: Comparison of photon azimuthal angle ϕ (left) and diphoton acoplanarity (right) of distributions obtained for different collision energies coming from SuperChic 4.2.

The transverse momentum $p_{\rm T}$ distributions of final-state photons are identical below 8 GeV. At higher values, small discrepancies start to appear, however they are likely due to limited statistical precision. No visible differences are observed in the pseudorapidity η of photon distributions, and the same holds for the photon azimuthal angle ϕ. For the diphoton acoplanarity, no discrepancies are seen at low values, where the statistical precision is highest, while some deviations appear in one bin with lower statistics. The

additional distributions shown in the Appendix are also consistent with each other, exhibiting only minor differences similar to those observed in the four example distributions discussed here.
Ratio of calculated cross sections from SuperChic 4.2 at 5.36 TeV to 5.02 TeV is:

$$\frac{\sigma_{5.36\ \text{TeV}}}{\sigma_{5.02\ \text{TeV}}} = \frac{132.46 \pm 0.54\ \text{nb}}{125.22 \pm 0.54\ \text{nb}} = 1.058 \pm 0.006,$$

which results in the 5.8% higher cross section obtained only from the increasing collision energy. Moreover, the same calculation is done using the UPCgen MC generator, however as the conclusion coming from results in shapes of distributions is the same, only a ratio of obtained cross sections are presented below:

$$\frac{\sigma_{5.36\ \text{TeV}}}{\sigma_{5.02\ \text{TeV}}} = \frac{123\ \text{nb}}{115\ \text{nb}} = 1.07$$ [1]

which gives a little bit larger than from SuperChic, about 7% greater cross section for Run 3 coming only from the collision energy increase.
Overall changing the collision energy does not change significantly shapes of presented here different kinematic distributions. This result therefore suggests that one does not need to worry about changing a plan of the analysis due to possible differences between data which could come from different collision energies available. At least for the collision energies studied in this thesis.

4.1.2 Ion breakup topologies

The zero-degree calorimeters (ZDCs) are located on both sides in the forward region of the ATLAS detector at 140 m from the interaction point and covers a pseudorapidity range above 8.3. They can measure neutral particles such as neutrons and photons.
In UPCs, the labels $0n0n$ and $XnXn$ refer to different nuclear-breakup topologies associated with the emission of forward neutrons. The exclusive $0n0n$ topology corresponds to events in which both ions remain intact after the electromagnetic interaction and no neutrons are emitted in either beam direction, resulting in no signal in the ZDCs. In contrast, the $XnXn$ topology denotes mutual possible nuclear breakup, where both ions undergo electromagnetic dissociation and emit one or more neutrons. Those neutrons can then be detected in the ZDCs on both sides of the interaction point due to their high-energy boost. In this thesis, the inclusive neutron category ($AnAn$) which contains every possible configuration: events in which the ions undergo nuclear breakup as well as those where both ions remain intact ($0n0n$) is compared with the $0n0n$ category.
LbyL scattering might be accompanied by a nuclear breakup. SuperChic MC generator is able to model forward neutron emission for every possible breakup topology. Since the ZDC signals are visible in UPC collisions by ATLAS, it is really helpful to make some predictions connected with this activity. In Figures 4.8-4.11 distributions for different variables for $AnAn$ and $0n0n$ topologies scaled to the data luminosity of 1.63 nb^{-1} are presented. The generated samples consist of 50 000 events each and have fiducial requirements of final-state photons: $p_{\text{T}} > 2$ GeV, $|\eta| < 2.5$ and $m_{\gamma\gamma} > 4$ GeV. It can be observed that differences between topologies are most pronounced in energy-related variables such as p_{T} and $m_{\gamma\gamma}$, whereas angular variables such as η and $\cos\theta^*$ show less sensitivity to the breakup topology. However in the case of $\cos(\theta^*)$ still, a slight dependence on the topology ratio can also be seen as the value of this variable increases.

[1] The UPCgen generator does not provide uncertainty of the cross section.

The ratio f_{0n0n} corresponds to $0n0n/AnAn_{(\text{total})}$ and represents the fraction of the cross section in which the nuclei remain intact and do not emit any neutrons. Obtained cross section from the generator for the ATLAS detector phase space can be used to calculate the predicted ratio of such topologies:

$$f_{0n0n} = \frac{\sigma_{0n0n}}{\sigma_{AnAn(\text{total})}} = \frac{108.33 \pm 0.04 \text{ nb}}{137.77 \pm 0.07 \text{ nb}} = 78.63 \pm 0.05\% \tag{4.5}$$

This result is consistent with the theoretical prediction of 75.3% reported in Ref. [20] within the possible model-dependent variations and fact that in this reference photon p_T starts at 2.5 GeV. For higher p_T one should expect a lower contribution from the $0n0n$ topology, therefore the result obtained in this thesis is consistent as it covers a slightly broader invariant mass range.
Studies of nuclear-breakup categories are important in the context of LbyL scattering as the selection of only $0n0n$ events can suppress a potential CEP ($gg \to \gamma\gamma$) background contribution for this process. This is justified by the fact that CEP in heavy ion UPCs is typically accompanied by nuclear excitation and therefore by neutron emission. In addition LbyL scattering is fully electromagnetic and preferentially occurs at high impact parameters, therefore it has a much higher probability to leave both nuclei intact ($0n0n$). As a result, requiring events with no activity detected on either side ($0n0n$) significantly reduces the CEP contribution, which predominantly populates the $XnXn$ topologies.

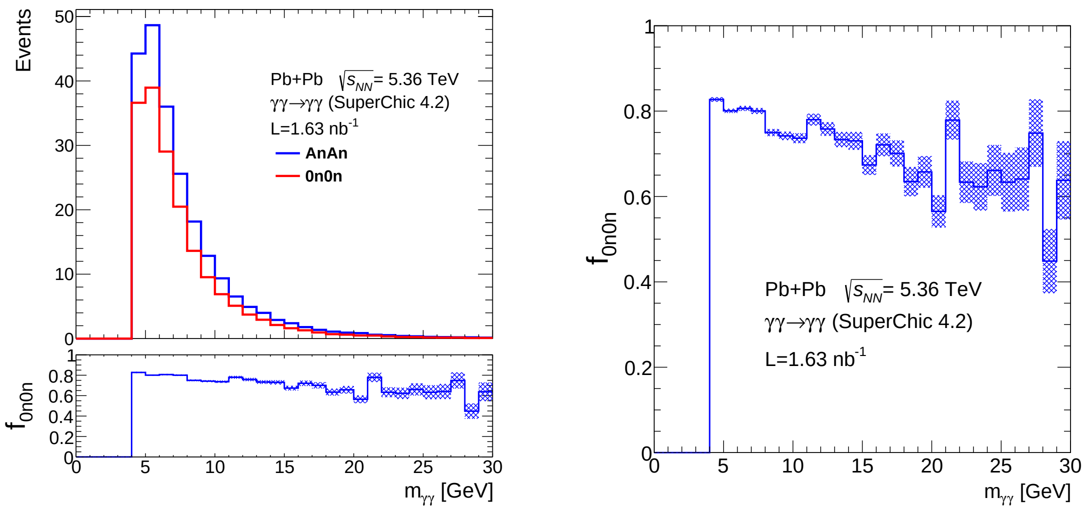

Figure 4.8: Comparison of diphoton invariant mass distributions for inclusive AnAn (total) and exclusive 0n0n ion breakup topologies for the $\gamma\gamma \to \gamma\gamma$ process coming from the SuperChic 4.2 MC generator. On right is enlarged ratio plot.

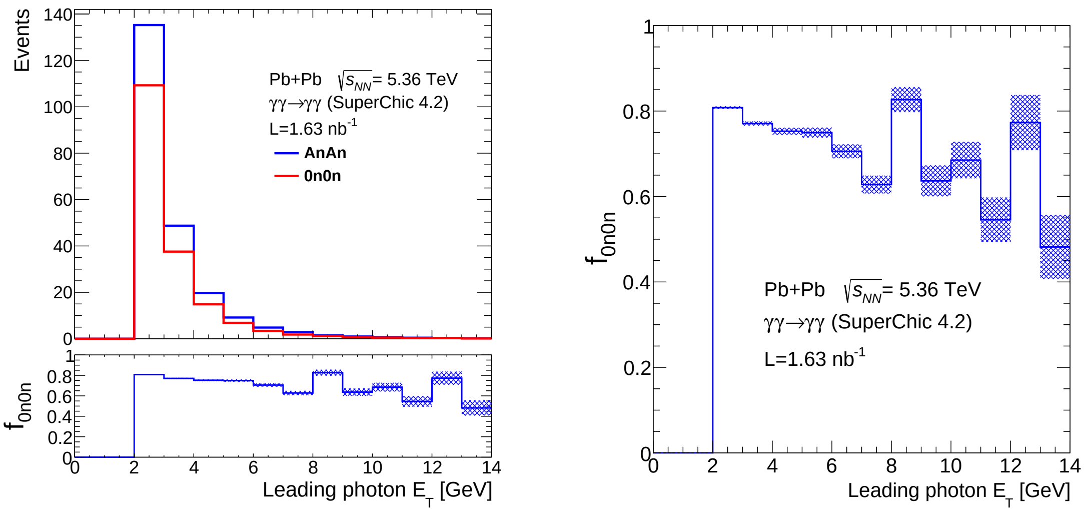

Figure 4.9: Comparison of leading photon p_T distributions for inclusive AnAn (total) and exclusive 0n0n ion breakup topologies for the $\gamma\gamma \to \gamma\gamma$ process coming from the SuperChic 4.2 MC generator. On right is enlarged ratio plot.

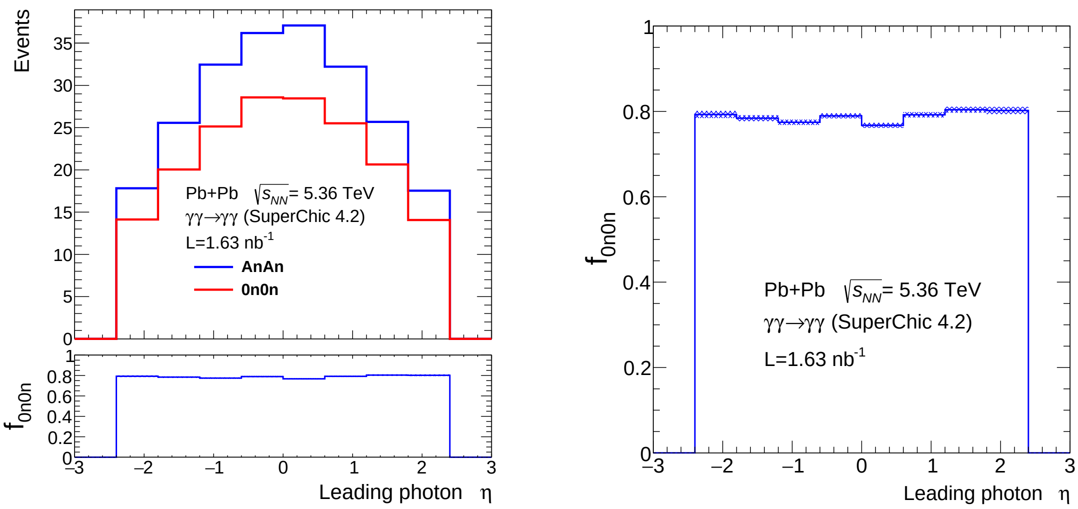

Figure 4.10: Comparison of leading photon η distributions for inclusive AnAn (total) and exclusive 0n0n ion breakup topologies for the $\gamma\gamma \to \gamma\gamma$ process coming from the SuperChic 4.2 MC generator. On right is enlarged ratio plot.

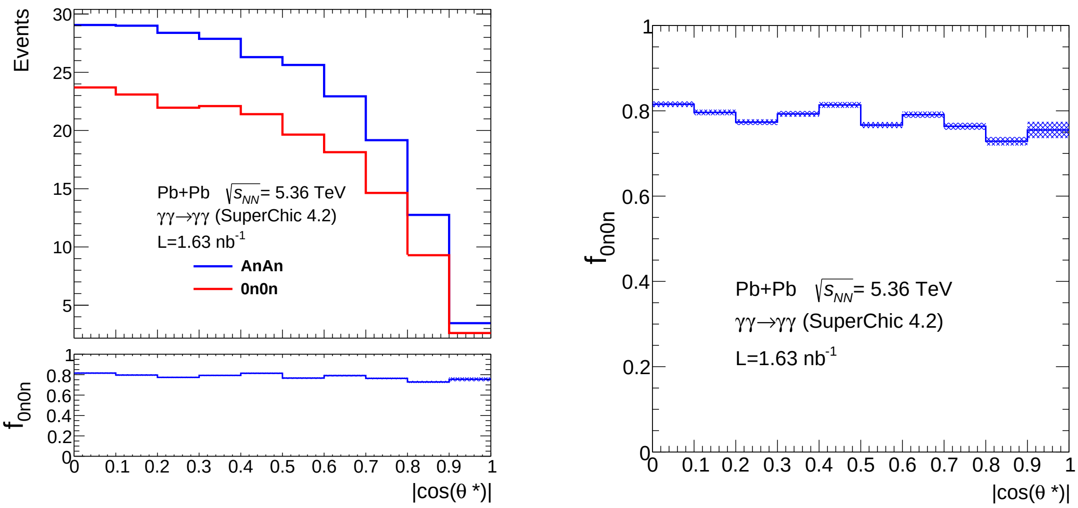

Figure 4.11: Comparison of $|\cos(\theta^*)|$ distributions for inclusive AnAn (total) and exclusive 0n0n ion breakup topologies for the $\gamma\gamma \to \gamma\gamma$ process coming from the SuperChic 4.2 MC generator. On right is enlarged ratio plot.

4.2 CEP background contribution

In precision studies of LbyL scattering at the LHC, a careful estimation of the background is essential. One of the dominant backgrounds arises from incoherent central exclusive production (CEP) of diphotons via the $gg \to \gamma\gamma$ process. Due to its different production mechanism, the CEP process exhibits kinematic properties that differ significantly from those of the LbyL signal. This allows the analysis to be divided into two distinct regions: a signal region dominated by LbyL events at low acoplanarity values, and a control region enriched in background contributions at larger acoplanarity. The control region is defined by the requirement on the diphoton acoplanarity:

$$\text{Aco} > 0.01.$$

This cut is optimized to give a high signal efficiency while significantly suppressing the CEP background, as the transverse momentum transferred in photon-induced interactions (which is in LbyL) is typically much smaller than that arising from gluon exchange (CEP) which leads to much lower diphoton acoplanarity values [21]. Generated samples are of 50 000 events for both processes with the fiducial requirements on final-state photons: $p_\text{T} > 2$ GeV, $|\eta| < 2.5$ and $m_{\gamma\gamma} > 4$ GeV at the centre-of-mass energy of 5.36 TeV. The cross section obtained from the generator is 10.567 ± 0.009 nb for the nominal PDF MMHT2015qed_nnlo (PDFs are discussed in more detail in the next subsection) - however this result is affected by a large theoretical uncertainty. In principle, a change of the generator version to new 5.6 leads to variations of the predicted cross section by up to an order of magnitude. In addition, the result shows a strong sensitivity to the choice of PDF set and PDF members.

After applying the control region requirement on the diphoton acoplanarity (> 0.01) from generated events, only 218 events remain for the LbyL process, while 32 867 events remain for the CEP process, highlighting the strongly back-to-back topology characteristic of the signal process. For the $gg \to \gamma\gamma$, older version of SuperChic (4.2) was used due to the major bug occurring in the newer version (5.3) where this process was not able to be generated. This process is subject to large theoretical uncertainties which are mainly related to the modelling of the rapidity gap survival probability. Therefore, all distributions in Figures 4.12-4.13 (and in additional Figure A.3 in Appendix) which present several control plots are shown normalised to 1 in order to compare only their shapes.

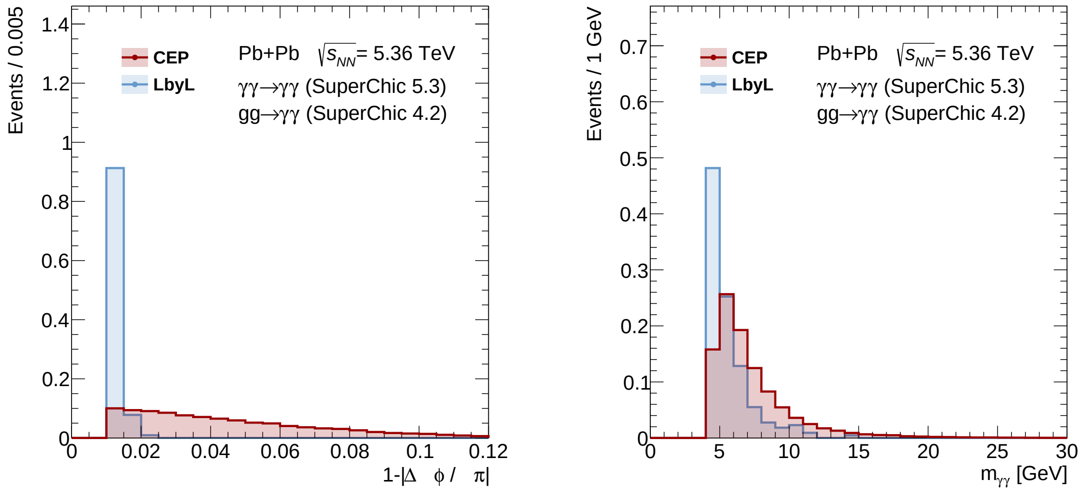

Figure 4.12: Comparison of diphoton acoplanarity (left) and diphoton invariant mass (right) shape distributions from LbyL scattering ($\gamma\gamma \rightarrow \gamma\gamma$) with incoherent CEP $gg \rightarrow \gamma\gamma$ process in the control region.

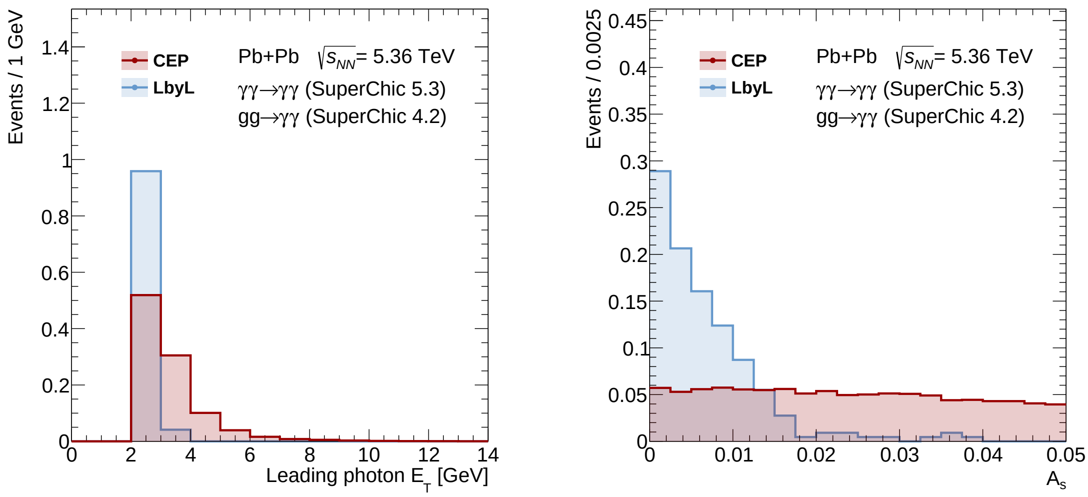

Figure 4.13: Comparison of leading photon p_{T} (left) and scalar asymmetry A_{S} (right) shape distributions from LbyL scattering ($\gamma\gamma \rightarrow \gamma\gamma$) with incoherent CEP $gg \rightarrow \gamma\gamma$ process in the control region.

In Figure 4.12 the acoplanarity distribution for LbyL events is strongly peaked at low values, reflecting (even after the Aco > 0.01 cut) the nearly back-to-back topology of the two photons characteristic of LbyL scattering. In contrast, the CEP process produces a significantly broader, nearly flat acoplanarity distribution which extends to higher values. The diphoton invariant mass distribution exhibits noticeable shape differences between the two processes, with CEP events showing a broader distribution extending to higher invariant masses. A similar conclusion can be drawn from the left panel of Figure 4.13, which shows the transverse momentum distribution of the leading photon. As expected, the behaviour is analogous to that observed for the invariant mass distribution as those are correlated. In addition, the scalar asymmetry distribution shown on the right panel of Figure 4.13 exhibits a qualitatively similar, though not identical, behaviour to that observed for the acoplanarity distribution. The scalar asymmetry distribution for the signal is broader, while the CEP background remains nearly flat, however at a higher level. While acoplanarity is primarily sensitive to the azimuthal imbalance of the diphoton system, the scalar asymmetry probes the imbalance in the transverse momenta of the two photons. Since the acoplanarity is correlated with the transverse momentum transferred in the interaction, the scalar asymmetry provides complementary sensitivity and in principle might also be used as a discriminating variable between the LbyL signal and the CEP background, in a manner similar to the acoplanarity variable.

4.2.1 CEP PDFs uncertainties

The predicted cross sections for the CEP process depend on the parton distribution functions (PDFs) of the nucleon, which describe the probability of finding a parton carrying a given fraction x of the nucleon momentum. Uncertainties in these PDFs therefore translate directly into uncertainties in the predicted CEP background.

To quantify these effects, the standard Hessian approach for PDF uncertainties is used. In this method, the PDF uncertainty is calculated along independent directions in the parameter space of the PDF set, called eigenvectors. Each eigenvector represents a main way in which the PDF can vary according to experimental constraints [22]. This method is particularly efficient for the moderate-size Hessian PDF sets as it makes it easy to see which directions contribute most to the total uncertainty.

For the estimation of uncertainties due to PDFs for the CEP $gg \to \gamma\gamma$ background process, two main sources are considered. The first one comes from the relative differences between nominal central PDF which is MMHT2015qed_nnlo and other PDFs. The second source is from PDF variations within the same PDF set (MMHT2015qed_nnlo) but for different PDF members. Table 4.1 shows names of all used PDFs in this analysis.

Table 4.1: List of PDFs used in calculation of CEP PDFs uncertainties.

PDF set name
MMHT2015qed_nnlo
TUJU21_nnlo_208_82
CT18ANLO
nCTEQ15HQ_FullNuc_208_82
EPPS21nlo_CT18Anlo_Pb208
nNNPDF30_nlo_as_0118_A208_Z82

For each PDF set and member, 50 000 events samples were produced with the same fiducial requirements corresponding to ATLAS fiducial region: $p_{\mathrm{T}}^{\gamma} > 2$ GeV, $|\eta^{\gamma}| < 2.5$, $m_{\gamma\gamma} > 4$ GeV at $\sqrt{s_{\mathrm{NN}}} = 5.36$ TeV, using the SuperChic 4.2 MC generator. For this estimation, the incoherent QCD-induced CEP was used.

Figure 4.14 shows normalised diphoton acoplanarity distributions for CEP $gg \to \gamma\gamma$ for each considered PDF in comparison to the nominal one. Acoplanarity variable is used as it is the most important variable for the LbyL analysis, as discussed in the previous section.

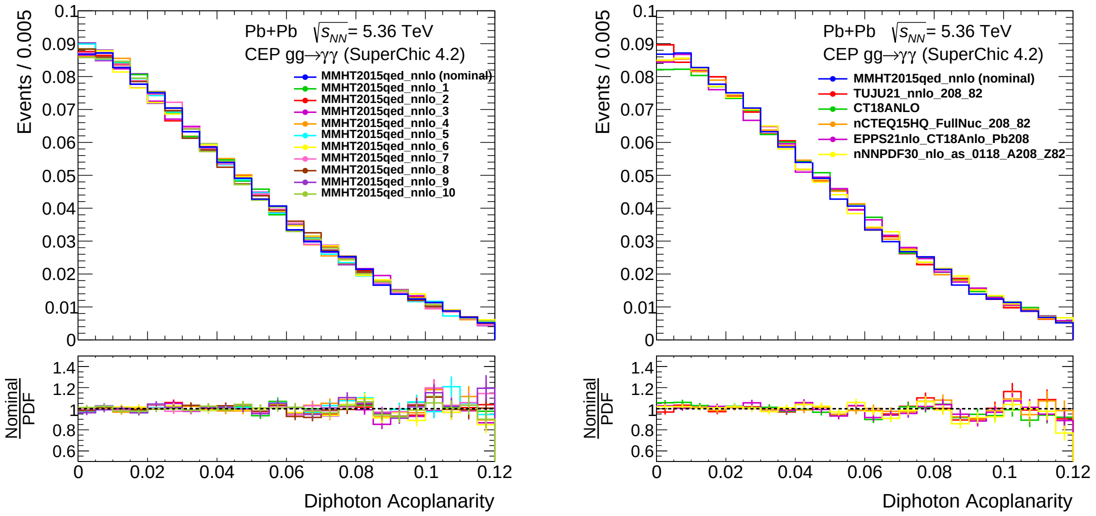

Figure 4.14: Effect of relative differences between nominal and its PDF members (left) and between nominal and other PDFs (right) on diphoton acoplanarity shape for CEP $gg \rightarrow \gamma\gamma$ process. On the bottom panels is the ratio of the nominal PDF to each PDF variation.

In order to calculate total uncertainty in each bin coming from every considered PDF variation, the formula below was used as suggested in the article [22]:

$$\delta\sigma = \sqrt{\sum_{k=1}^{N_{mem}} (\sigma^{(k)} - \sigma^{(0)})^2}, \tag{4.6}$$

where $\sigma^{(k)}$ is the value in a given bin for the k-th PDF variation and $\sigma^{(0)}$ corresponds to the nominal PDF. This approach follows the standard Hessian prescription for PDF uncertainties, which estimates the total uncertainty by considering independent directions in the PDF parameter space. Each direction, represented by an eigenvector of the Hessian matrix, corresponds to a principal mode of variation constrained by experimental data, allowing one to assess how variations in the underlying parton distributions propagate to the observable cross sections.
After using formula (4.6) one can obtain the following graphs with calculated errors in each given bin of acoplanarity distribution. Such result showing total uncertainties is presented in Figure 4.15.

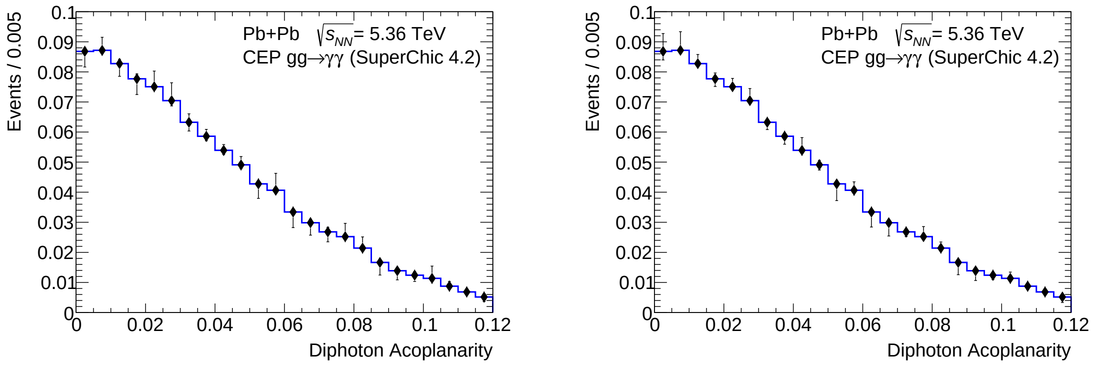

Figure 4.15: Total uncertainty coming from differences between nominal and its PDF members (left) and between nominal and other PDFs (right) on diphoton acoplanarity shape for CEP $gg \to \gamma\gamma$ process.

To propagate these uncertainties further, it is necessary to calculate the relative significance of the error in each bin. The resulting uncertainties range from 0-25% for acoplanarity values below 0.1, increasing for higher acoplanarity. Therefore these contributions coming from different PDFs in the CEP $gg \to \gamma\gamma$ process are not negligible and have to be considered in the analysis of real data.

4.3 Dipion production

In UPCs of heavy ions, quasi-real photons emitted from the electromagnetic fields of the colliding nuclei may interact to produce a pair of neutral pions ($\gamma\gamma \to \pi^0\pi^0$). Theoretical estimates published prior to Run 2, suggested that the cross section for this rare exclusive dipion production lies in the range of 1-100 pb [23, 10]. The production of a neutral pion pair, is particularly interesting because pions are mesons, therefore they probe the hadronic structure of the photon and involve non-perturbative QCD dynamics at low invariant masses. From the experimental point of view, in LbyL analysis, dipion production was not analysed before in great details as measured diphoton invariant masses were above 5 GeV. However, in the recent ATLAS analysis, the accessible diphoton invariant mass range has been extended down to $m_{\gamma\gamma} = 4$ GeV, probing a lower energy region compared to the previous LbyL scattering measurements. This lower-mass window brings the study closer to the transition between perturbative and non-perturbative QCD regimes, where hadronic two-photon processes such as $\gamma\gamma \to \pi^0\pi^0$ may become increasingly relevant. Exploring this domain therefore is necessary because it is sensitive to new, previously unexplored kinematic regions in heavy-ion UPC analyses which can impact the whole analysis and conclusions from it.

Dipion production can potentially contribute as background for the signal (LbyL scattering) process. Precisely, neutral pions primarily decay into two photons, so in the final state where dipion production occurred, a total of four photons are expected ($\pi^0\pi^0 \to (\gamma\gamma)(\gamma\gamma)$). Such a process can mimic the LbyL diphoton signal if two out of the four photons are outside the detector's acceptance or if the pairs of photons originating from the same pion are reconstructed as a single electromagnetic cluster with higher energy. Therefore, estimating the contribution of this process to the LbyL signal region is essential for LbyL measurements.

To consider the two scenarios as potential contributions to the background of LbyL ATLAS analysis, MC simulations are performed using the UPCGEN generator. The MC cross section obtained from the generator is 90 nb in Pb-Pb collisions at $\sqrt{s_{\rm NN}} = 5.36$ TeV with the selection criteria filtered according to the ATLAS acceptance: $p_{\rm T}^{\pi} > 2$ GeV and $|\eta^{\pi}| < 2.5$. To better understand the properties of dipions in the process $\gamma\gamma \to \pi^0\pi^0$, Figures 4.16-4.21 present key kinematic distributions of neutral pions and their decay photons at the generator level.

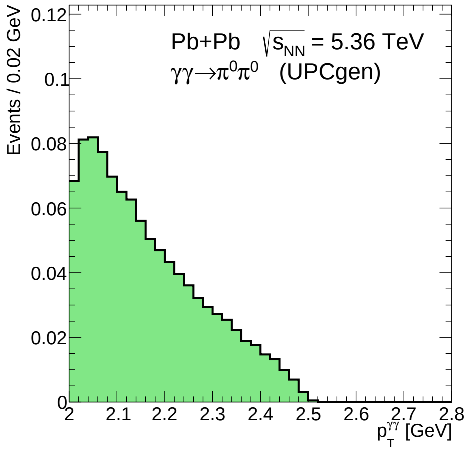

Figure 4.16: Transverse momentum distribution of neutral pions (photon pairs) at the generator level.

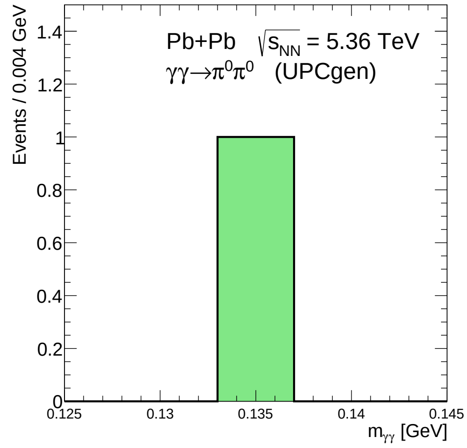

Figure 4.17: Invariant mass distribution of photons originating from the same pion at the generator level.

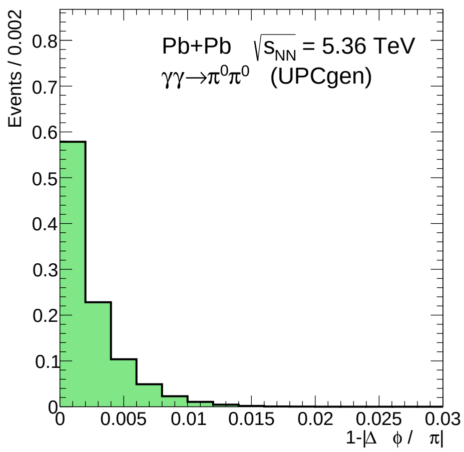

Figure 4.18: Acoplanarity distribution of neutral pion pairs at generator level.

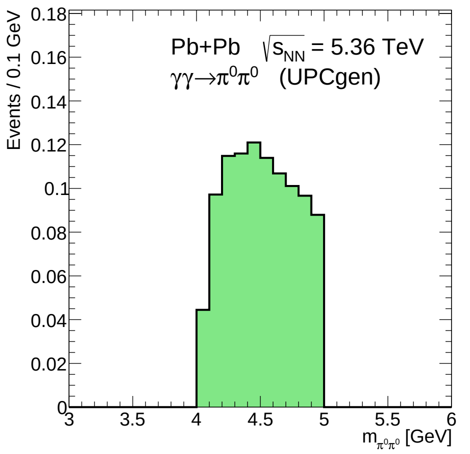

Figure 4.19: System invariant mass ($m_{\pi^0\pi^0}$) distribution of neutral pions at the generator level.

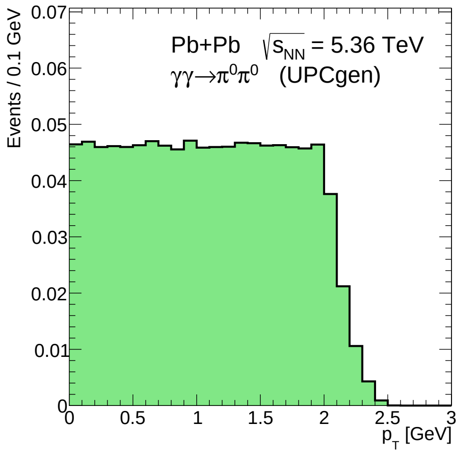

Figure 4.20: Transverse momentum distribution of photons originating from pions at the generator level.

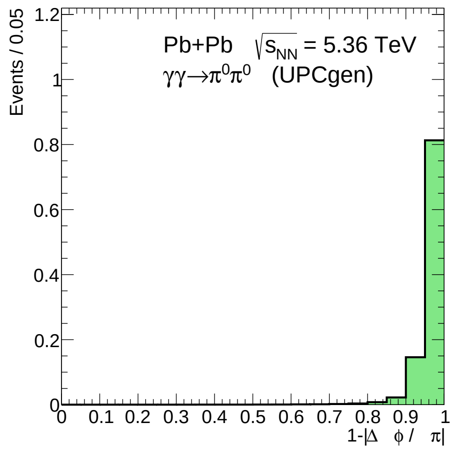

Figure 4.21: Acoplanarity distribution of photon pairs originating from the same pion at the generator level.

Figure 4.16 shows the total transverse momentum (p_{T}) distribution of photons pairs originating from the same neutral pion. In other words it shows the distribution of transverse momentum of the created pions ($p_{\mathrm{T}}^{\pi^0}$), illustrating the typical kinematic range of generated pions. Figure 4.17 displays the invariant mass of photon pairs from the same pion. As expected, the distribution peaks sharply at the nominal neutral pion mass of approximately 135 MeV, however without any visible broadening. This behavior reflects the idealized nature of the generator, which does not include detector effects such as energy resolution. The acoplanarity distribution of pion pairs, shown in Figure 4.18, demonstrates that most pions created in events exhibit very small acoplanarity values, confirming the predominantly back-to-back production characteristic of the exclusive $\gamma\gamma \to \pi^0\pi^0$ process. Figure 4.19 shows the invariant mass distribution of the produced dipion system (or equivalently, of the four photons originating from their decays). As expected, the distribution starts at around 4 GeV, which is consistent with the minimum transverse momentum $p_{\mathrm{T}}^{\pi^0}$ threshold set in the generator. However, as the number of events decreases with increasing invariant mass, a sharp cutoff appears at 5 GeV. This behaviour will be more described later. Next, Figure 4.20 presents the transverse momentum distribution of all photons originating from both pions. Again, a sharp cutoff is visible near 2.5 GeV, which is consistent with the previous observation of the cutoff at 5 GeV in invariant mass. Finally, the last plot shows the acoplanarity distribution, this time not for the pions themselves but for photon pairs originating from the same parent pion. The distribution reaches large values, peaking close to the maximum of 1, indicating that the produced photons are emitted very close to each other in angular phase space.

The first background topology considered, which could originate from the $\pi^0\pi^0 \to (\gamma\gamma)(\gamma\gamma)$ process, is the so-called photon merging. This scenario assumes that two photons from the same parent pion are sufficiently close to each other in phase space that the detector reconstructs them as a single electromagnetic cluster (topo-cluster) with higher total energy. Such cases are expected to be relatively common, since in the UPCGEN generator sample, the produced pions have transverse momenta of $p_{\mathrm{T}}^{\pi} > 2$ GeV as seen in Figure 4.16, which by definition corresponds to the vector sum of the transverse momenta of their daughter photons.

However, to evaluate this effect, it is necessary to examine the angular separation between individual photons originating from the same parent pion. This can be quantified using the $\Delta\mathrm{R}$ variable:

$$\Delta\mathrm{R} = \sqrt{(\Delta\varphi)^2 + (\Delta\eta)^2}, \tag{4.7}$$

which measures the spatial distance between two particles in the detector's pseudo-rapidity-azimuthal angle space. Here, $\Delta\varphi$ is the difference in azimuthal angle, and $\Delta\eta$ is the difference in pseudorapidity between the two photons. The smaller the value of $\Delta\mathrm{R}$, the closer the photons are to each other, making them more difficult to distinguish experimentally. Assuming a separation cut of $\Delta\mathrm{R} < 0.2$, approximately 30,000 out of 50,000 generated events fulfill this condition, corresponding to a relatively large cross section for such configurations. However, it is essential to compare this with the spatial resolution of the ATLAS electromagnetic calorimeter, which defines the minimum angular distance at which two nearby photons can still be resolved as distinct clusters. This resolution is smaller than $\Delta\mathrm{R} = 0.1$, depending on the region of the detector. Figure 4.22 shows the distribution of $\Delta\mathrm{R}$ between photons originating from the same parent pion for all generated events at the truth MC level.

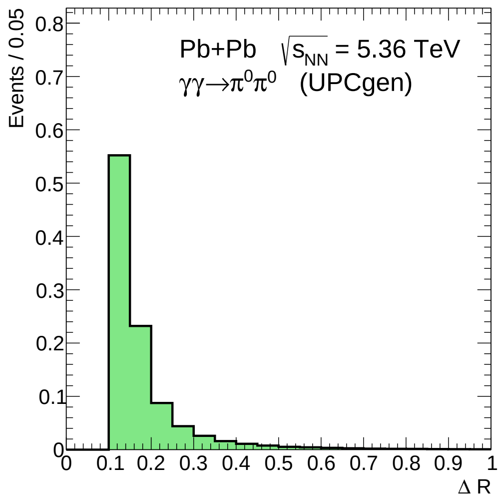

Figure 4.22: The $\Delta\mathrm{R}$ distribution of photon pairs ($\gamma\gamma$) at the generator level originating from the decay of the same pion in dipion production.

The distribution starts at around $\Delta\mathrm{R} = 0.1$, above the detector's resolution threshold. Consequently, the ATLAS calorimeter should be capable of separating both photons in nearly all cases as events start slightly above $\Delta\mathrm{R} = 0.1$, reconstructing them as two distinct clusters rather than a merged single one. Moreover, since photons from the same pion are emitted in close proximity, the probability of one of them escaping the detector's acceptance while the other is detected is extremely low (except possibly at the acceptance edges). Therefore, in principle, one should always observe four distinct photons in the final state. However, no events with four reconstructed photons are observed in data. Photons must be identified using the BDT working point. None of the events pass this selection in the data, which is surprising given the relatively large generator-level cross section.

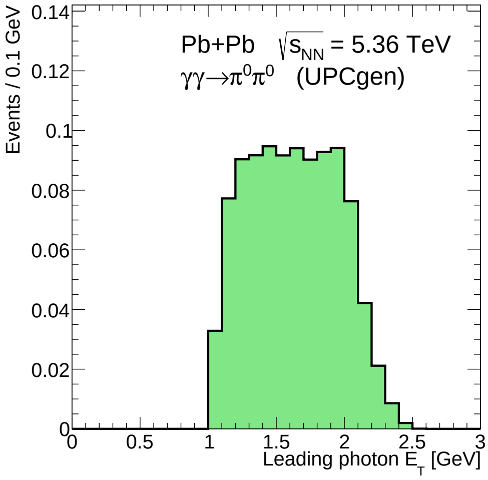

Figure 4.23: Transverse momentum distribution of the leading photon originating from first pion.

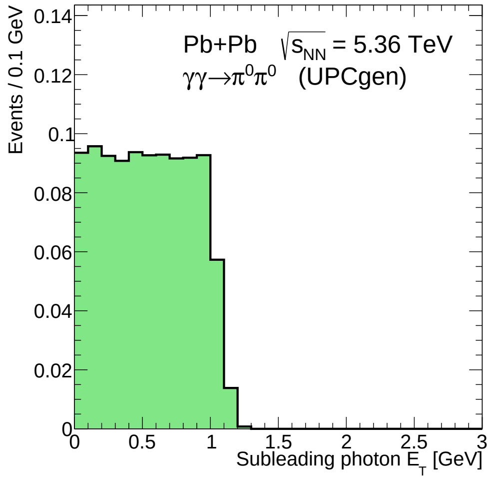

Figure 4.24: Transverse momentum distribution of the subleading photon originating from first pion.

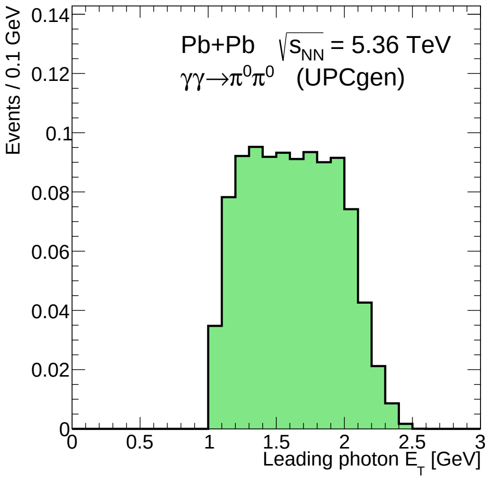

Figure 4.25: Transverse momentum distribution of the leading photon originating from second pion.

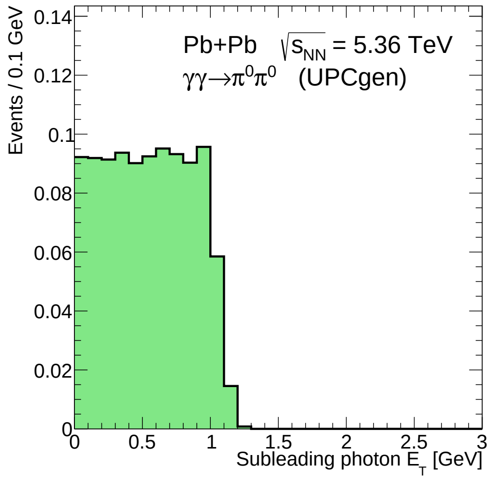

Figure 4.26: Transverse momentum distribution of the subleading photon originating from second pion.

Figures 4.23-4.26 show the transverse momentum distributions for the leading and subleading photons originating from each pion (pion 1 and pion 2). It is evident that the leading photon always populates higher p_T values than the subleading one. Recalling that the minimal p_T required for photon reconstruction is 2 GeV, it follows that the majority of photons fall below this threshold. The distributions also demonstrate that, within each pion pair, one of the two photons fails to reach the required energy. These observations imply that when applying a photon selection threshold of $p_T > 2$ GeV, events with three or four reconstructed photons will effectively never appear - consistent with what is observed in data. In addition, there is an additional cutoff applied to the dipion invariant mass (< 5 GeV), which will affect this selection.

As a result, the only observable topology that could mimic the LbyL signal is the case where one photon from each pion satisfies the $p_{\mathrm{T}} > 2$ GeV requirement, leading to a two-photon final state. The number of such events surviving the selection is approximately 1600, corresponding to a cross section of $\sigma \approx 2.9$ nb. For an integrated luminosity of the data set collected by ATLAS of 1.63 nb^{-1}, this yields an expectation of about 4-5 events in both the control and signal regions defined in Section 4.2. In addition, the estimated cross section for the $\pi^0\pi^0 \to (\gamma\gamma)(\gamma\gamma)$ process, where only one photon from each pion is detected, is approximately 0.25 nb in the control region defined by Aco > 0.01. This corresponds to fewer than one expected event for the integrated luminosity of the dataset (1.63 nb^{-1}). In contrast, the cross section in the signal region is about 4 nb, as the majority of the events fall within this region, yielding roughly 4-5 expected events.
Figure 4.27-4.32 presents several kinematic distributions for these selected events. As can be seen from the acoplanarity and total transverse momentum ($p_{\mathrm{T}}^{\mathrm{total}}$) distributions shown in Figures 4.31 and 4.32, the two photons are produced almost back-to-back, reflecting the production kinematics of the parent pions. Consequently, most of these events would populate the signal region, as indicated by the calculated cross sections, emphasizing the relevance of this background component. In Figure 4.27, all events are found in the range of 2-3 GeV, which is also clearly a consequence of the upper invariant mass limit imposed by the generator ($m_{\pi^0\pi^0} < 5$ GeV) - the same behaviour can be observed in Figure 4.29. Figures 4.28 and 4.30 additionally present the angular distributions of the selected events. Overall, the presented distributions serve as control plots for the LbyL analysis. Their binning is chosen to match that used in the main analysis, and the obtained shapes roughly correspond to what is "missing" in the measured data. However, due to the generator cut at $m_{\pi^0\pi^0} < 5$ GeV, the distributions do not extend to the next invariant-mass bin, and the resulting shapes may therefore be slightly distorted.

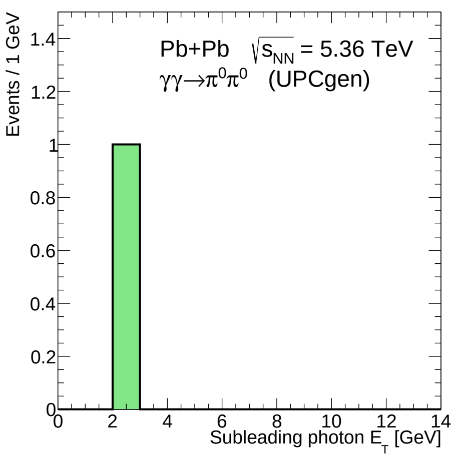

Figure 4.27: Subleading photon transverse momentum distribution for events selected in the observable topology at generator level.

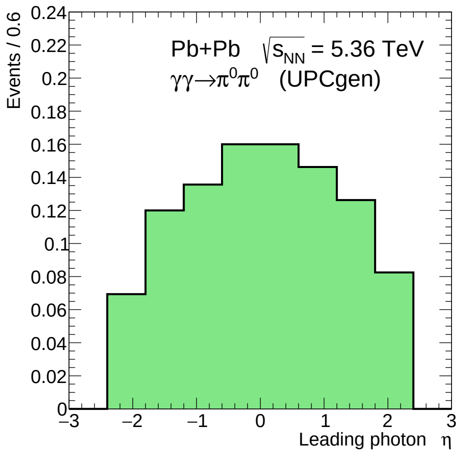

Figure 4.28: Leading photon pseudorapidity distribution for events selected in the observable topology at generator level.

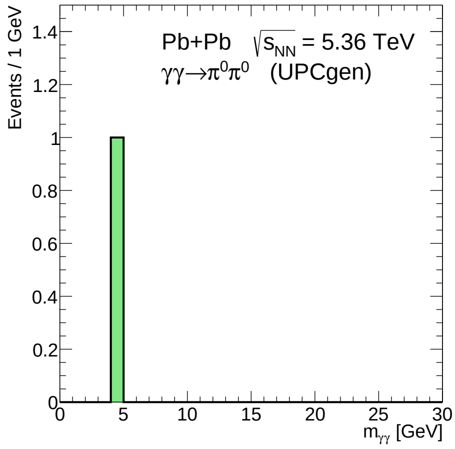

Figure 4.29: Invariant mass distribution of photons for events selected in the observable topology at generator level.

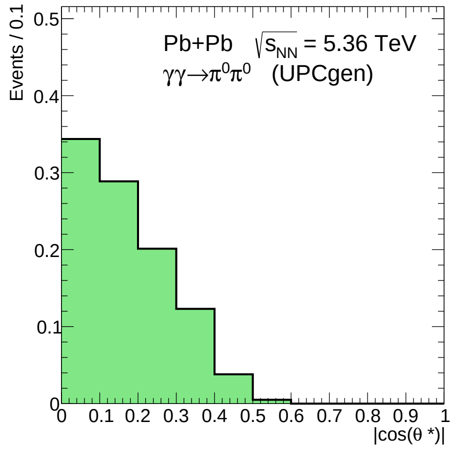

Figure 4.30: $|\cos(\theta^*)|$ distribution of photons for events selected in the observable topology at generator level.

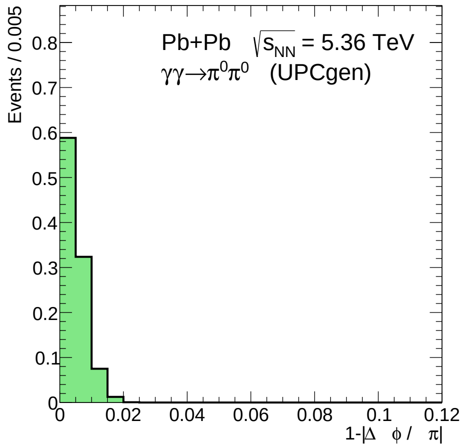

Figure 4.31: Acoplanarity distribution of photons for events selected in the observable topology at generator level.

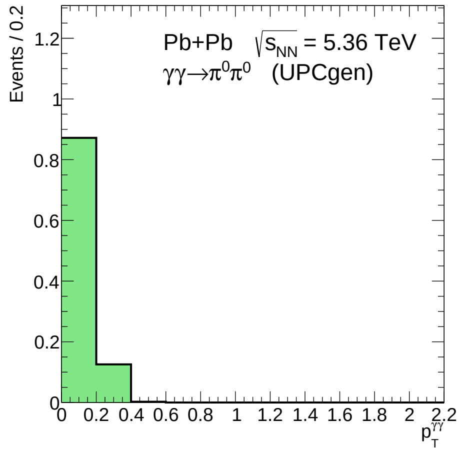

Figure 4.32: Total transverse momentum of photons for events selected in the observable topology at generator level.

The mentioned mass cutoff at 5 GeV originates from the generator itself - in the $\gamma\gamma \to \pi^0\pi^0$ process generation, a fixed upper cut of $m_{\pi^0\pi^0} < 5$ GeV is applied by the authors of UPCGEN. This limit is likely introduced to focus on the low-mass region (below 5 GeV), where the process is phenomenologically interesting and the background becomes relevant. It also reflects the rapidly decreasing cross section at higher invariant masses, although such a restriction may not be optimal for the present analysis. In Figure 4.33 the generator-level cross section as a function of the applied minimum pion transverse momentum ($p_T^{\pi^0}$) cut is shown.

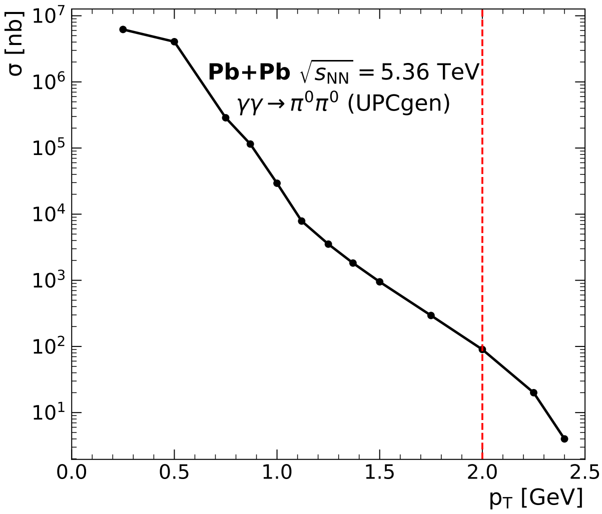

Figure 4.33: MC cross section from UPCgen generator vs minimum transverse momentum p_{T} threshold for the process of dipion production. This analysis used threshold marked with the red line.

It can be seen that the cross section decreases rapidly with increasing p_{T}, a fact also reflected in the significantly longer generation time required for samples with higher cuts. As the cut increases, fewer and fewer events can be produced, eventually reaching the upper kinematic limit corresponding to $p_{\mathrm{T}}^{\pi^0} \approx 2.5$ GeV (or an invariant mass of 5 GeV). A gradual decrease of the invariant mass distribution between 4 and 5 GeV is also visible, followed by as said a cut at 5 GeV. If this constraint was lifted, the distribution might probably continue its smooth falloff beyond 5 GeV, consistent with the expected decrease of the photon-photon luminosity and the rapidly dropping cross section at higher invariant masses. However, such events would be extremely rare due to the very small production probability at those energies, but still this fact can be problematic for the analysis made in the range of masses also greater than 5 GeV.

4.4 Other rare processes

The process $\gamma\gamma \rightarrow e^+e^-\gamma\gamma$, which contains four particles in the final state as a result of final-state radiation (FSR), can also be a potential background to the LbyL scattering signal process. This happens when only two out of the four final-state particles are reconstructed as photons in the detector acceptance. Since the described process is more complicated, it is also more difficult to simulate it accurately and it is not available in standard UPC MC generators such as SuperChic or STARlight [24]. In order to simulate such processes, one example of a generator that can handle them is MadGraph5.
First the $\gamma\gamma \rightarrow e^+e^-$ process was successfully simulated in MadGraph5 and used as a reference to validate the order of magnitude of the calculated cross sections. The obtained cross section amounts to $\sigma(\gamma\gamma \rightarrow e^+e^-) = (4.29 \pm 0.05) \times 10^8$ pb, corresponding to approximately 429 μb, which is in reasonable agreement with previous expectations and earlier Run 2 studies, where values of the order of 200 μb were reported after applying analysis-level kinematic selections [25]. Then the process $\gamma\gamma \rightarrow e^+e^-\gamma\gamma$ was also simulated with fiducial requirements: $p_{\mathrm{T},e} > 2$ GeV, $|\eta_e| < 2.5$, $\Delta R_{ee} > 0.01$, $\Delta R_{\gamma\gamma} > 0.01$, and $\Delta R_{e\gamma} > 0.01$. Its cross section was found to be $\sigma(\gamma\gamma \rightarrow e^+e^-\gamma\gamma) = (9.95 \pm 0.06)$ nb.

The ratio of the cross sections of the four-particle final state to the leading-order dilepton process is therefore:

$$\frac{\sigma(\gamma\gamma \to e^+e^-\gamma\gamma)}{\sigma(\gamma\gamma \to e^+e^-)} \approx 2.3 \times 10^{-5},$$

indicating a strong suppression of this higher-order process. Although the pure $\gamma\gamma \to \gamma\gamma$ process could not be generated within the same framework due to technical reasons, a comparison with predictions from SuperChic shows that the relative magnitude of the cross sections is consistent. The ratio of the $\gamma\gamma \to e^+e^-\gamma\gamma$ cross section obtained with MadGraph5 to the $\gamma\gamma \to \gamma\gamma$ cross section predicted by SuperChic amounts to

$$\frac{9.95 \text{ nb}}{138 \text{ nb}} \approx 0.07,$$

which indicates that the $\gamma\gamma \to e^+e^-\gamma\gamma$ process contributes approximately 7% additional events relative to the total $\gamma\gamma \to \gamma\gamma$ signal.
However taking into account the limited detector acceptance and reconstruction efficiency for multi-particle final state, its contribution to the selected event sample is expected to be negligible. In particular, the probability that such events pass the trigger requirements and are reconstructed as exclusive two-photon candidates is further reduced by the performance of the trigger system and photon identification criteria. Therefore, this process does not constitute a significant background to the LbyL scattering measurement and can be safely neglected in the analysis.

5. Analysis of real UPC data in ATLAS

In the ATLAS experiment, the trigger system is responsible for selecting interesting events in real time from the large number of collisions delivered by the LHC. It consists of two levels: Level-1 (L1), a hardware-based trigger performing a fast initial selection, and the High-Level Trigger (HLT), a software-based system providing refined event selection using full detector information. The vpix60 selection is part of the ATLAS HLT system and is designed to select low-multiplicity UPC Pb-Pb events efficiently, reducing the rate of background events with higher track multiplicities. Its proper calibration and efficiency measurement are crucial for analyses relying on precise event selection, such as LbyL scattering studies.
For studies of HLT efficiency estimation, vpix60 selection can be used. It imposes a veto on the number of hits in the pixel detectors more than 60 per event. The selection was designed in addition to diphoton events efficiently select also exclusive dielectron events ($\gamma\gamma \rightarrow e^+e^-$) with two tracks on average. A high value of the veto is due to increasing noises in the detector as it is getting older. In this section the vpix60 efficiency is studied in the UPC data stream collected in the collisions of Pb-Pb ions in November 2025. Only runs 00511115-00511617 are used in the analysis. This results in lower recorded statistics of events than total collected lumi in this period of time and, as a result, makes uncertainties slightly bigger. In the studies the OR of two supporting HLT triggers for the vpix60 veto is considered:

- HLT_mb_sptrk_hi_FgapAC5_L123INVM_27DPHI_2eTAU1_VjTE200,
- HLT_mb_sptrk_hi_FgapAC5_L1DPHI_2eTAU1_VjTE200.

The efficiency of the HLT vpix60 trigger is obtained by dividing the number of events satisfying the condition that the total number of pixel hits in the barrel region and both endcaps of the ATLAS Inner Detector is below 60 by the total number of events without this requirement. This procedure provides a direct estimate of efficiency of the vpix60 trigger (which is just a cut in the nominator). This efficiency is later evaluated as a function of the rapidity of the electron-positron pair that pass the selection for the $\gamma\gamma \rightarrow e^+e^-$ process.
The selection criteria for the $\gamma\gamma \rightarrow e^+e^-$ process used are described below:

- Exactly two electrons with:
  - $p_{\mathrm{T}} > 2$ GeV,
  - $|\eta| < 2.47$, excluding the "crack" region ($1.37 < |\eta| < 1.52$),
- Opposite electric charges (e^+e^-),
- Dielectron acoplanarity Aco < 0.02.

Moreover, an event with both electrons must pass an OR of supporting HLT triggers for the efficiency calculations. The total number of events obtained after applying the selection criteria and using the logical OR of the supporting triggers is 27524. Figures 5.1 and 5.2 show control plots for $\gamma\gamma \rightarrow e^+e^-$ candidates that passed these requirements.

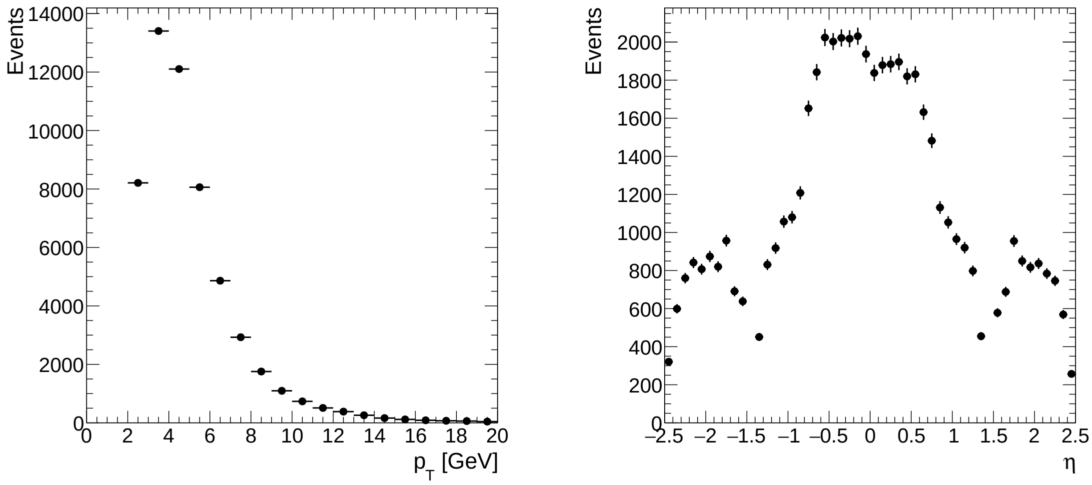

Figure 5.1: Electron transverse momentum p_{T} (left) and electron pseudorapidity η (right) for $\gamma\gamma \to e^{+}e^{-}$ event candidates obtained from collected data (2025) used to calculate the vpix60 trigger efficiency.

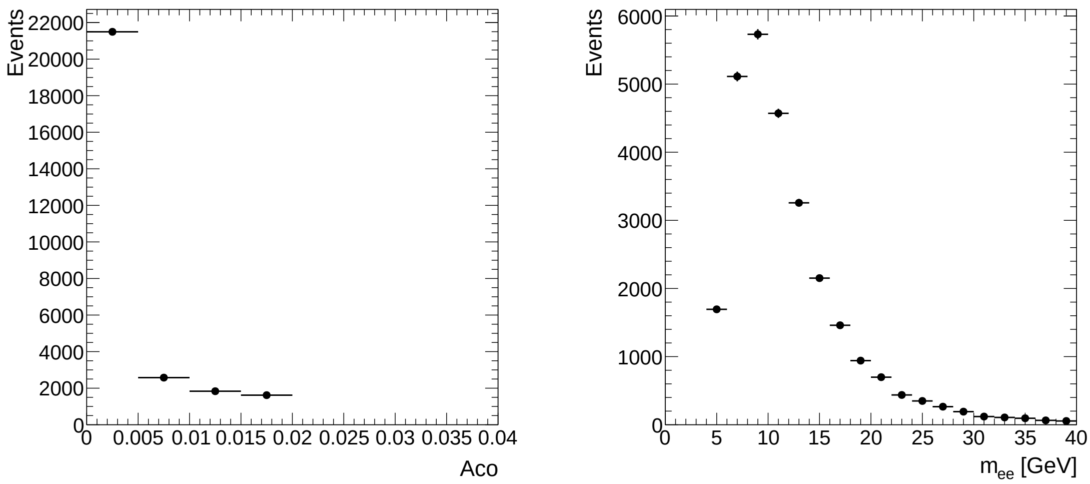

Figure 5.2: Dielectron acoplanarity Aco (left) and dielectron invariant mass m_{ee} (right) for $\gamma\gamma \to e^{+}e^{-}$ event candidates obtained from collected data (2025) used to calculate the vpix60 trigger efficiency.

The transverse momentum of electrons originating from the $e^{+}e^{-}$ process, shown on the left-hand side of Figure 5.1, starts at 2 GeV, in agreement with the applied selection criteria. The electron pseudorapidity distribution shown on the right-hand side of the same Figure is also consistent with these requirements. Figure 5.2 (left) shows that the dielectron acoplanarity is peaked at zero and below 0.02, as required by the applied cut. In addition, the invariant mass distribution of the electron-positron pair is shown (right); as expected, it starts at 4 GeV. Then the cut for numbers of pixel hits is applied in order to calculate the nominator of the efficiency:

$$\varepsilon_{\text{vpix60}} = \frac{N_{\text{pixel hits} < 60}}{N_{\text{all pixel hits}}}. \tag{5.1}$$

In the initial stage of this analysis, no explicit selection on the activity of topo-clusters was applied, as such effects were expected to be negligible for exclusive $\gamma\gamma \to e^+e^-$ events in UPCs in contrast to the 2023 data analysis where this requirement was present [26]. However, a more detailed inspection revealed the presence of an additional background component in 2025 data. This additional activity becomes evident when studying the correlation between the pixel hit multiplicity and the topo-clusters multiplicity. Figure 5.3 shows the two-dimensional distributions used to investigate activity of topo-clusters for events passing the dielectron selection and OR of supporting triggers.

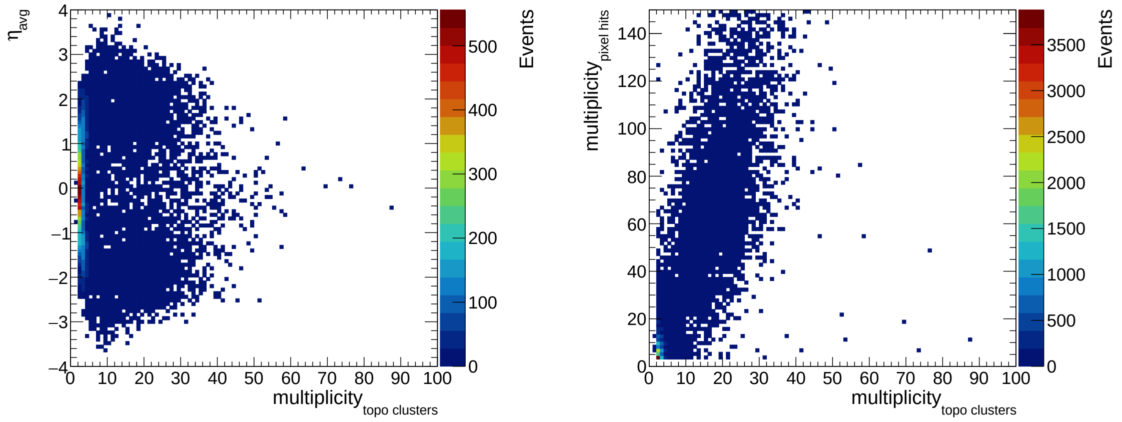

Figure 5.3: Two-dimensional distributions of topo-cluster activity for events passing selection criteria of $\gamma\gamma \to e^+e^-$ and OR of supporting triggers: the topo-cluster multiplicity versus the average topo-cluster pseudorapidity (left) and the topo-cluster multiplicity versus the pixel hit multiplicity (right).

On the left of Figure 5.3, one can see the average pseudorapidity of the topo-cluster η_{avg}, as a function of its multiplicity. In 2023, symmetrical activity in both directions of η_{avg} was more clearly separated [26]. However, the results obtained for 2025 data show increased activity also around the central values of average topo-cluster pseudorapidity. On the right, one can observe a clear dependence of the total number of pixel hits (used to calculate the vpix60 efficiency) on the multiplicity of the topo-cluster. Consequently, it is necessary to impose an additional requirement on topo-cluster activity to suppress the visible background and noise. Therefore, in this analysis events must have a maximum multiplicity of topo-clusters of:

- $\text{multiplicity}_{\text{topo cluster}} < 10$.

This requirement effectively removes events with enhanced calorimeter activity while preserving the bulk of the exclusive signal. After introducing the topo-cluster cut, the final total number of events passing the $\gamma\gamma \to e^+e^-$ selection, with an OR of the supporting triggers and the topo-cluster multiplicity cut applied, is 22115.

An obtained distribution of the number of pixel hits in events passing the dielectron selection and OR of supporting trigger with an additional topo-cluster requirement is shown in Figure 5.4. A composite function consisting of Landau distribution, exponential and 3rd degree polymonial is fitted to the data. The Landau function models the main peak while the exponential describes a tail of high-multiplicity events and detector noise. The third-order polynomial is used to absorb fluctuations and shape asymmetries due to lower statistics.

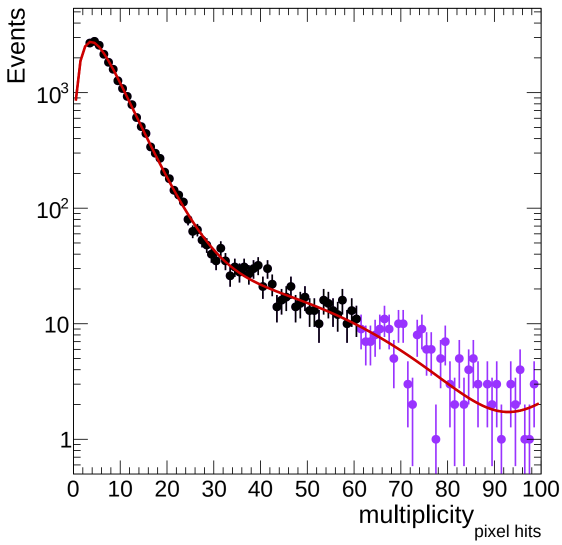

Figure 5.4: Distribution of number of pixel hits passing the selection requirements of $\gamma\gamma \rightarrow e^+e^-$ with vpix60 triggers (HLT). Combination of Landau, exponential and 3rd degree polynomial functions fitted in red. Purple data points mark events with more than 60 pixel hits.

The main peak of the pixel hits multiplicity distribution is located around ~ 4.5 hits, as obtained from the fit, and extends up to approximately 30 hits. The core of the distribution corresponds to ionizing particle deposits from electron tracks in UPC events. Beyond this, the distribution develops a relatively flat tail, which can arise from higher-multiplicity events, detector noise which still remains after the topo-cluster cut or overlapping hits from nearby tracks. The fit approaches 2 around 90 pixel hits, above the vpix60 veto. A parameter χ^2/ndf value of 1.23 is considered acceptable, indicating reasonable agreement between the fitted function and the observed data within statistical uncertainties.
The vpix60 trigger efficiency, as mentioned before, is studied in $\gamma\gamma \rightarrow e^+e^-$ event candidates as a function of dielectron rapidity. Of course, besides satisfying the electron-positron selection criteria, an OR of two supporting triggers is applied, together with added cut requiring the topo-cluster multiplicity to be less than 10. The measured efficiency is shown in Figure 5.5. It is very close to unity, varying in the range from 0.987 ± 0.002 to 0.995 ± 0.003 across the rapidity spectrum.

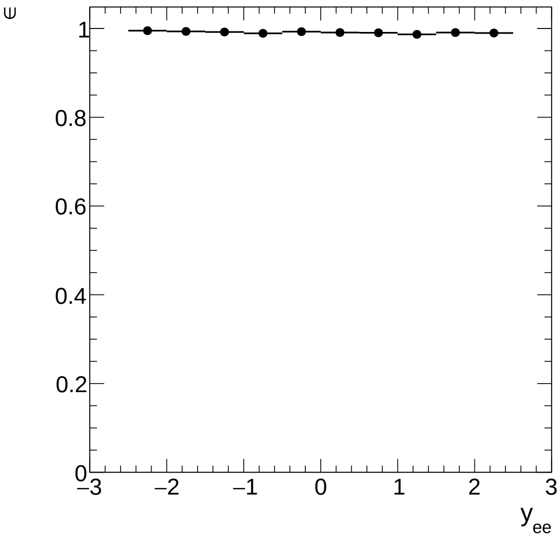

Figure 5.5: Efficiency of the vpix60 selection as a function of dielectron rapidity y_{ee}.

Overall, the study demonstrates that the vpix60 trigger is reliable and well-suited for selecting low-multiplicity events in Pb-Pb UPCs. Its efficiency is very high, close to 1, reflecting the stable performance of the pixel detector. This makes the trigger highly effective for physics analyses requiring clean event selection with minimal background contamination. However, this result can only be achieved when the additional topo-cluster cut is applied, as otherwise an extra unidentified background is observed, indicated by the dependence of the pixel-hit multiplicity on the topo-cluster multiplicity. This effect still requires further investigation; therefore, a more optimized topo-cluster selection must be developed, which will require additional studies.

6. Theoretical predictions for ALICE detector's phase space

6.1 Motivation

This section presents an extension of the Author's results reported in [27].
The ALICE experiment at the LHC has undergone significant upgrades to its detector systems, which now enable a broader range of measurements in UPCs of lead nuclei. During Run 3 and Run 4, integrated luminosities of $L = 7$ nb^{-1} and 6 nb^{-1}, respectively, are expected, providing unprecedented opportunities to study rare processes with high precision. One of the most intriguing phenomena accessible in these collisions (which was already discussed in the ATLAS context) is LbyL scattering.
While LbyL scattering has already been observed by ATLAS [4, 6] and CMS [5] experiments in kinematic regions corresponding to diphoton invariant masses $m_{\gamma\gamma} > 5$ GeV and photon rapidities $|\eta| < 2.4$, it has never been measured in the ALICE experiment. A main aspect which makes the ALICE detector different is that it provides a unique opportunity to explore this process in lower invariant mass ranges ($m_{\gamma\gamma} < 5$ GeV) in the central barrel region. Studying LbyL scattering in this previously unexplored kinematic domain is motivated by the desire to test Standard Model predictions in a new regime and to probe photon-photon interactions with sensitivity to possible contributions from physics beyond the Standard Model.
As said, the upgraded ALICE detector, including the electromagnetic calorimeters (EMCal and PHOS) and the tracking devices (TPC and ITS), provide high-resolution measurements in the central rapidity region similar to ATLAS or CMS experiments. However, the planned installation of the Forward Calorimeter (FoCal) during Long Shutdown 3 (2026-2030) will extend the experiment's coverage into the forward rapidity region. This combination allows not only for a comprehensive study of LbyL scattering in a lower invariant mass regime but also across both central and forward kinematic regions, enabling access to a novel phase space that was previously inaccessible.
To provide realistic predictions for these potential future measurements in the ALICE experiment, MC simulations are used. In this work, two widely used generators, SuperChic 5.4 and UPCgen, are employed to simulate the LbyL process. The simulations take into account the full acceptance of the current and future detectors and analyze all possible reconstruction topologies. Comparing results across different generators and topologies allows for a detailed assessment of expected yields, kinematic distributions, and systematic uncertainties, which is essential for designing future analyses and optimizing the experimental strategy.
Overall, this work is motivated by the combination of ALICE's upgraded detector capabilities (forward calorimeter FoCal), the opportunity to explore a new invariant mass range for LbyL scattering, and therefore the potential to deepen our understanding of photon-photon interactions in heavy-ion collisions. By providing detailed predictions and exploring the sensitivity of various detector configurations, this study lays the groundwork for the first measurement of LbyL scattering in ALICE, complementing the existing results from ATLAS and CMS and extending the exploration of this rare process to previously uncharted kinematic regions.

6.2 Signal process

To describe the prospects for measuring LbyL scattering within ALICE's unique invariant mass range, one first needs to determine whether a significant signal is expected and, if so, how many events can be observed. The signal process $\gamma\gamma \rightarrow \gamma\gamma$, within the ALICE phase space, is simulated using two MC generators: SuperChic 5.4 and UPCgen, with the following fiducial requirements: pseudorapidity $|\eta| < 0.9$, minimum transverse momentum of the scattered photon $p_{\mathrm{T}}^{\gamma} > 0.3$ GeV, diphoton invariant mass $m_{\gamma\gamma} > 0.5$ GeV, and full azimuthal coverage.

Several reconstruction topologies are possible, depending on the detector region in which the photons are detected. The energy deposit of the electromagnetic cascade, produced by the incident photon in the calorimeter, can be measured directly or alternatively using the Photon Conversion Method (PCM) [28], in which the photon is reconstructed from an electron-positron pair produced via photon conversion in the detector's material with 8.5% probability (5% was assumed in this analysis). In the central rapidity region, the Electromagnetic Calorimeter (EMCal) [29] and the Photon Spectrometer (PHOS) [30] can be considered to measure photon signal. The EMCal covers the ranges $|\eta| < 0.68$ and $80^\circ < \phi < 187^\circ$, or $0.22 < |\eta| < 0.7$ and $260^\circ < \phi < 320^\circ$, or $|\eta| < 0.7$ and $320^\circ < \phi < 327^\circ$, with a minimum photon transverse momentum of $p_{\mathrm{T}}^{\mathrm{min}} = 0.5$ GeV and $p_{\mathrm{T}} > 2.5$ GeV for the EMCal trigger. The PHOS covers $|\eta| < 0.13$ and $70^\circ < \phi < 190^\circ$, with $p_{\mathrm{T}}^{\mathrm{min}} = 0.3$ GeV. Photons can also be reconstructed using the PCM method over the full azimuth and within $|\eta| < 0.9$. However, only about 5% of signal photons are registered due to the limited conversion probability. For PCM, a minimum transverse momentum of $p_{\mathrm{T}}^{\mathrm{min}} = 0.5$ GeV is applied.

In summary both signal photons from the LbyL scattering process must be registered either in EMCal, PHOS, or reconstructed by PCM. Hybrid cases are also possible, for example, when one photon falls within the EMCal acceptance while the other is detected in PHOS. Therefore, the accessible detection topologies are: EMCal + EMCal, EMCal + EMCal (trigger), PCM + PCM, EMCal + PHOS, EMCal + PCM, and PHOS + PCM. The PHOS + PHOS topology is not accessible due to its limited acceptance and a predicted number of events below 1.

Besides of the central region, the installation of the Forward Calorimeter (FoCal) is planned for Long Shutdown 3 [31]. The FoCal, designed as a cuboidal detector, will be positioned approximately 7 meters from the interaction point, covering the forward rapidity range of $3.2 < \eta < 5.8$. It consists of two parts: a hadronic section, FoCal-H, and an electromagnetic section, FoCal-E. The electromagnetic section, FoCal-E, will be employed for the detection of photon-photon final states. The minimum transverse momentum of photons is set to $p_{\mathrm{T}}^{\mathrm{min}} = 0.5$ GeV.

Two acceptance scenarios are considered for the FoCal: the full configuration and a reduced configuration, in which four modules are removed from each side, to illustrate the impact on the predicted signal yield. In both scenarios, both photons from the LbyL scattering process are required to fall within the FoCal's forward rapidity acceptance. A schematic view of the electromagnetic part of FoCal; FoCal-E geometry is shown in Figure 6.1. In this figure, two rectangular contours - drawn in yellow and red - are added to illustrate the full FoCal area considered in the signal counting. These contours represent the limits in the y coordinate ($|y| < 31.2$ cm and $|y| < 50.5$ cm, respectively) and thus include the entire FoCal acceptance. This approach allows for a more precise estimation of the number of detectable signal events, since pseudorapidity boundaries correspond to circular (conical) contours in spatial coordinates, whereas the FoCal geometry is rectangular in x-y space

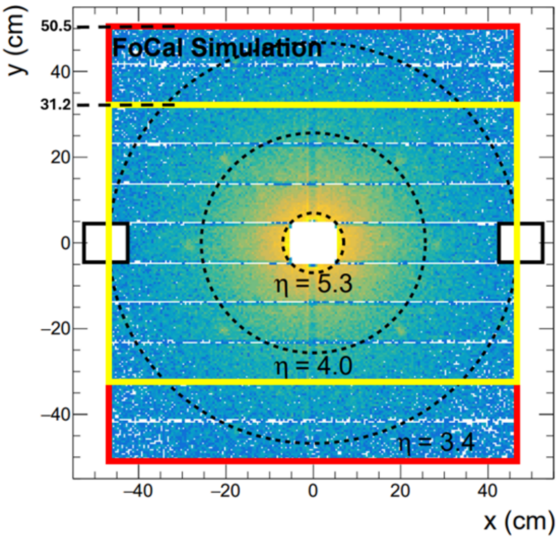

Figure 6.1: Spatial distribution of reconstructed photon clusters in FoCal-E. Dashed circles represent contours of fixed pseudorapidity. The yellow rectangle indicates the contour corresponding to $|y| < 31.2$ cm, while the red one corresponds to $|y| < 50.5$ cm [31].

The generated events are analysed for all possible reconstruction topologies, as described, in both the central and forward rapidity phase spaces.
Figure 6.2 presents the expected LbyL scattering signal yield in the central barrel region of the ALICE detector, evaluated for an integrated luminosity of $\mathcal{L} = 13$ nb^{-1} predicted to be in both Run 3 and Run 4, using SuperChic and UPCgen MC generators. Different color (not black) distributions correspond to all considered distinct topologies in which two final-state photons can be detected; therefore, their sum represents the total observable signal yield, while the black dots correspond to all generated events. Considering both plots, although the initial distributions differ slightly in their high invariant mass tails, both generators predict similar yields in the low invariant mass region; consequently, the color-marked considered topologies are in good agreement. Obtained cross sections from both generators for the signal process are $\sigma^{\mathrm{SC}} = 2332 \pm 1$ nb and $\sigma^{\mathrm{UPCgen}} = 2538$ nb for SuperChic and UPCgen, respectively.

The total number of events with $m_{\gamma\gamma} < 10$ GeV that satisfy the selection criteria for all considered topologies (described previously) is 1147 ± 34 and 1232 ± 35 for SuperChic and UPCgen, respectively. From both distributions one can see that the event yield increases with decreasing diphoton invariant mass which is expected. Therefore, in order to measure interesting rare signal processes such as LbyL scattering, it is crucial to attempt lowering the measurable energy threshold which will improve event statistics.

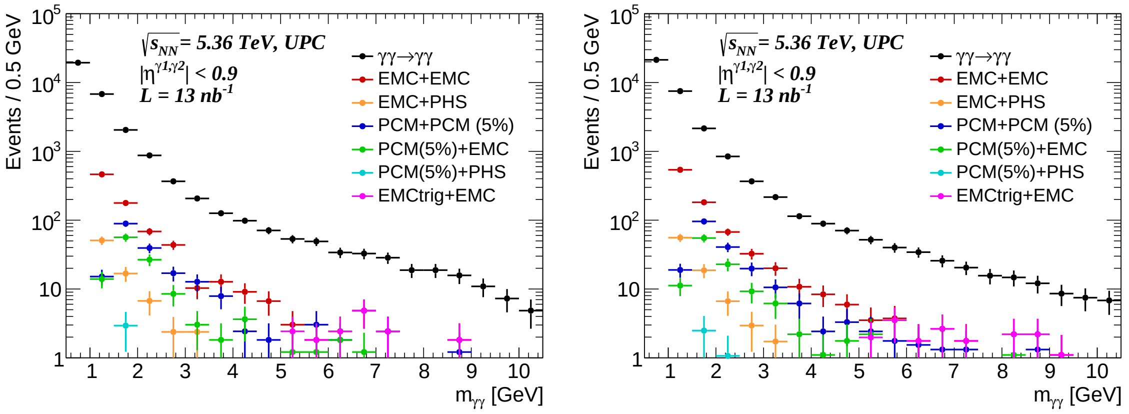

Figure 6.2: Expected LbyL scattering yield measured in different topologies in the ALICE detector in the central region for $\mathcal{L} = 13$ nb^{-1} as a function of the diphoton invariant mass coming from SuperChic 5.4 (left) and UPCgen (right) MC generators.

Similar results are obtained for the forward region described previously and presented in Figure 6.3. In this case obtained cross sections from the MC generators are $\sigma^{\text{SC}} = 216.92 \pm 0.07$ nb for SuperChic and $\sigma^{\text{UPCgen}} = 165.55$ nb for UPCgen. The number of events within the full FoCal acceptance (blue lines) are 1074 ± 33 for SuperChic and 925 ± 30 for UPCgen, therefore they are slightly more different. Similarly as in the case of the central region, here a number of events increases as the invariant mass goes down.
When comparing the invariant mass range in the forward region to that in the central region, a significantly smaller yield is expected in the forward phase space. The number of events above $m_{\gamma\gamma} = 2$ GeV remains only around 80 for both MC generators which is several times smaller than for the case of the central region.

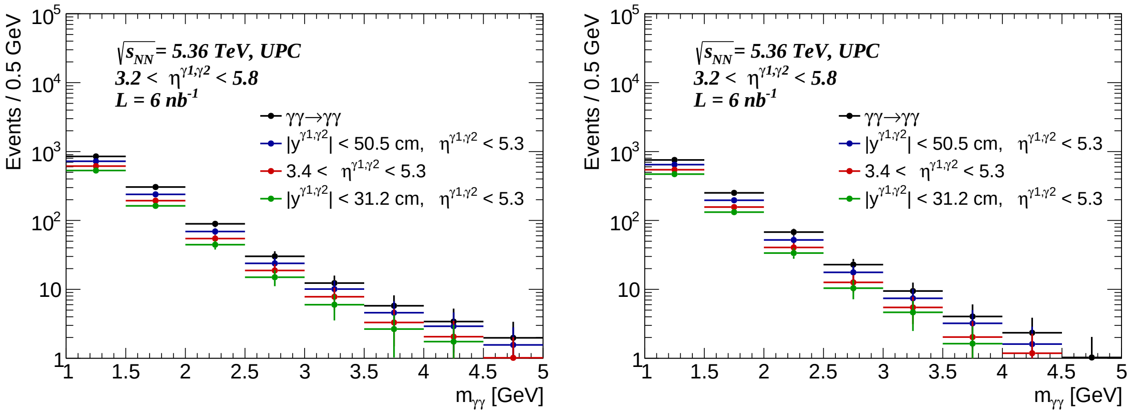

Figure 6.3: Expected LbyL scattering yield measured in different topologies in the ALICE FoCal detector in the forward region for $\mathcal{L} = 6$ nb^{-1} as a function of the diphoton invariant mass coming from SuperChic 5.4 (left) and UPCgen (right) MC generators.

The expected LbyL scattering yields in the ALICE central barrel and forward FoCal regions are summarized in Tables 6.1-6.3. Table 6.1 presents the central barrel results predicted by SuperChic for an integrated luminosity of $\mathcal{L} = 13$ nb^{-1}, while Table 6.2

shows the corresponding predictions from UPCGEN. Both generators indicate that the largest yields occur in the lower invariant mass region, with the total number of events across all topologies slightly higher for UPCGEN than for SUPERCHIC. The dominant contributions come from the EMCAL and PCM + EMCAL topologies, whereas PHOS alone does not register any events.

Table 6.1: Expected LbyL scattering yield measured in different topologies in the ALICE detector in the central region for different detector topologies with an integrated luminosity of $\mathcal{L} = 13$ nb^{-1} predicted by SUPERCHIC. Cross section $\sigma^{\mathrm{SC}} = 2332 \pm 1$ nb and 50 000 generated events.

Topology	$m_{\gamma\gamma} < 10$ GeV	Total (without $m_{\gamma\gamma}$ cut)
ALL (generated)	30273	30319
PCM	198	198
EMCAL	810	814
PHOS	0	0
EMCAL + PHOS	362	364
PCM + EMCAL	121	122
PCM + PHOS	5	22
EMCAL trigger	18	22

Table 6.2: Expected LbyL scattering yield measured in different topologies in the ALICE detector in the central region for different detector topologies with an integrated luminosity of $\mathcal{L} = 13$ nb^{-1} predicted by UPCGEN. Cross section $\sigma^{\mathrm{UPCgen}} = 2538$ nb and 150 000 generated events.

Topology	$m_{\gamma\gamma} < 10$ GeV	Total (without $m_{\gamma\gamma}$ cut)
ALL (generated)	32955	32994
PCM	210	212
EMCAL	888	890
PHOS	0	0
EMCAL + PHOS	395	397
PCM + EMCAL	116	117
PCM + PHOS	5	22
EMCAL trigger	19	22

The forward region results are reported in Tables 6.3 and 6.4 for SUPERCHIC and UPCGEN, respectively, for an integrated luminosity of $\mathcal{L} = 6$ nb^{-1}. The event yields are given for three diphoton invariant mass thresholds: $m_{\gamma\gamma} > 1$, 2, and 4 GeV. As expected, the number of events decreases with increasing invariant mass and is generally lower than in the central barrel region, reflecting the reduced phase space in the forward rapidity region. The largest contributions are observed in the widest acceptance intervals ($3.2 < \eta < 5.3$ and $|y| < 50.5$ cm), whereas the smallest yields correspond to the narrowest rapidity ranges and highest invariant mass thresholds. Comparing the obtained yields for the reduced configuration ($|y| < 31.2$ cm) with those for the full planned FoCal-E surface, it is evident that the number of events decreases by approximately 30%. Furthermore, when considering the prediction for $4.3 < \eta$, which corresponds to the collinear phase space of the reduced surface ($|y| < 31.2$ cm), the number of events drops significantly. This highlights the importance of accurately taking into account the detector surface using the full x-y coordinates.

Table 6.3: Expected LbyL scattering yield in the forward region of the ALICE detector for different detector topologies, predicted by SuperChic, with an integrated luminosity of $\mathcal{L} = 6$ nb^{-1}. Cross section $\sigma^{\text{SC}} = 216.92 \pm 0.07$ nb and 50 000 generated events.

Topology	$m_{\gamma\gamma} > 1$ GeV	$m_{\gamma\gamma} > 2$ GeV	$m_{\gamma\gamma} > 4$ GeV
ALL (generated)	1 298	95	3
$\|y\| < 50.5$ cm	1 074	81	3
$3.4 < \eta < 5.3$	896	65	2
$\|y\| < 31.2$ cm	764	52	2
$4.3 < \eta < 5.3$	142	6	0

Table 6.4: Expected LbyL scattering yield in the forward region of the ALICE detector for different detector topologies, predicted by UPCgen, with an integrated luminosity of $\mathcal{L} = 6$ nb^{-1}. Cross section $\sigma^{\text{SC}} = 165.55$ nb and 50 000 generated events.

Topology	$m_{\gamma\gamma} > 1$ GeV	$m_{\gamma\gamma} > 2$ GeV	$m_{\gamma\gamma} > 4$ GeV
ALL (generated)	1 114	71	2
$\|y\| < 50.5$ cm	925	59	2
$3.4 < \eta < 5.3$	763	46	1
$\|y\| < 31.2$ cm	654	38	1
$4.3 < \eta < 5.3$	111	4	0

From the comparison of central and forward regions, it is evident that the expected event yield in the forward acceptance is significantly smaller than in the barrel, particularly for $m_{\gamma\gamma} > 2$ GeV, where only a few tens of events are predicted. These results highlight the importance of lowering the detector energy thresholds and maximizing the acceptance in order to enhance the statistics for rare processes such as LbyL scattering. Furthermore, the comparison between SuperChic and UPCgen indicates that while the absolute yields in the central region differ only slightly, the forward region exhibits more pronounced discrepancies between the two generators. Predictions for the central region are consistent in the low invariant mass range, 1 GeV $< m_{\gamma\gamma} <$ 5 GeV, whereas noticeable differences appear in the forward rapidity region covered by FoCal. The spectra, as well as the ratios of the predicted invariant mass distributions from both generators, are shown in Figure 6.4.

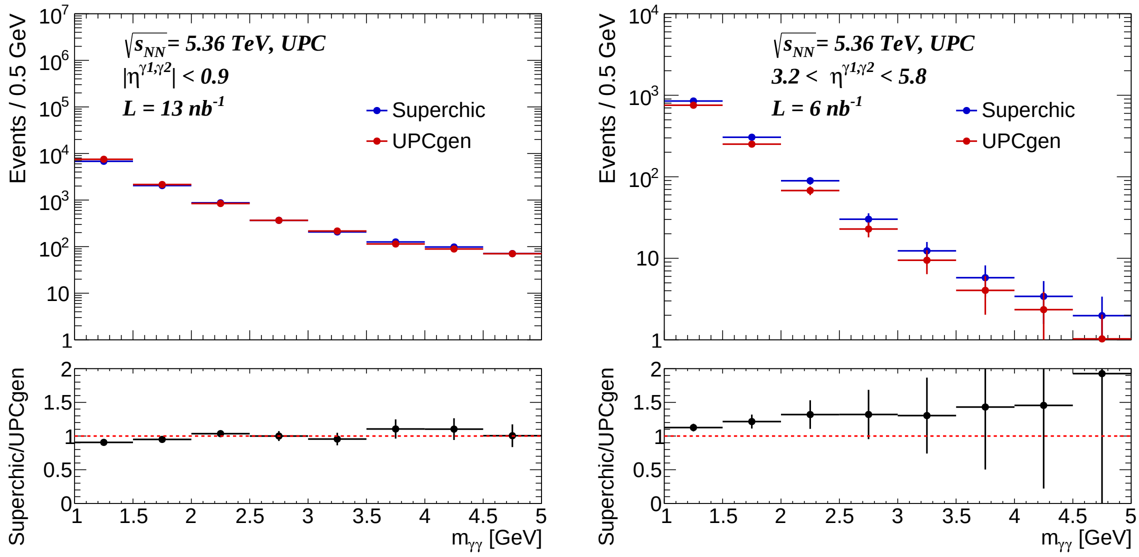

Figure 6.4: Top panels: Comparison of the diphoton invariant mass spectra generated by SuperChic 5.4 and UPCgen MC generators for the central region (left-hand side) and forward (right) region. Bottom panels: The ratio of predicted yield by SuperChic 5.4 to UPCgen MC generators.

In the top panels of Figure 6.4, the diphoton invariant mass spectra generated by SuperChic 5.4 and UPCgen are compared for the central region (left) and forward region (right). The bottom panels show the ratio of the yields predicted by SuperChic 5.4 to those from UPCgen.

While the ratio remains close to unity in the central region, it deviates significantly in the forward region, starting from the lowest invariant mass and exhibiting an increasing trend. Although the higher-mass bins are affected by large statistical uncertainties due to low event counts, the overall rising trend persists, indicating a systematic difference rather than mere statistical fluctuations. These discrepancies are likely caused by the different photon flux models employed by the two generators.

Based on the predictions from both SuperChic 5.4 and UPCgen, the total expected number of LbyL scattering events, summing over the central barrel and forward FoCal regions and applying the fiducial selection criteria, is approximately 2310 ± 48 for SuperChic and 2254 ± 47 for UPCgen. These numbers represent ideal estimates, assuming perfect detector efficiency, no additional experimental constraints, and the maximum integrated luminosity achievable over Runs 3 and 4. The event yields are highest in the low invariant mass region, particularly below $m_{\gamma\gamma} \sim 5$ GeV, and decrease both with increasing invariant mass and in the forward rapidity acceptance, where the phase space is smaller. Despite the differences observed between the generators, the overall trends are consistent, indicating that measurements of LbyL scattering in the ALICE detector are feasible.

However, these predictions reflect the signal only. The actual number of measurable events may be lower due to experimental factors such as detector efficiency, achievable integrated luminosity, and the presence of background contributions. Therefore, while the signal yields alone suggest that studying LbyL scattering is worthwhile, a full feasibility study must also include detailed evaluations of backgrounds, efficiency of detectors, triggers etc. Nonetheless, the predicted event rates are promising and justify pursuing a dedicated measurement of this rare process, particularly in the low invariant mass region where the sensitivity is highest.

6.3 Dominant backgrounds

Having established the expected signal yields, we shall turn our attention to the predicted contributions from background processes, which are crucial for assessing the overall feasibility and significance of the measurement.

6.3.1 Dipion production

In the dipion production process, $\gamma\gamma \to \pi^0\pi^0 \to (\gamma\gamma)(\gamma\gamma)$, as the reader already knows from previous chapters, each neutral pion promptly decays into two photons, resulting in a four-photon final state. This background is particularly dominant at low invariant masses, which are precisely the region of interest for ALICE due to its unique acceptance. To simulate this kind of background the UPCGEN MC generator is used with the following fiducial requirements which reflect central (barrel) and forward (FoCal) acceptance of the ALICE detector in Pb-Pb collisions at $\sqrt{s_{\mathrm{NN}}} = 5.36$ TeV: $p_{\mathrm{T}}^{\pi} > 0.3$ GeV, $|\eta^{\pi}| < 0.9$ for the central region and $p_{\mathrm{T}}^{\pi} > 0.5$ GeV, $3.2 < \eta^{\pi} < 5.8$ for the forward, FoCal phase space. The obtained MC cross sections are 326.67 ± 0.07 μb for the forward FoCal region and 1602.55 ± 0.31 μb for the central Barrel region.
At sufficiently high pion transverse momentum, the two decay photons may become merged and therefore be reconstructed as a single electromagnetic cluster in the detector. However, in the kinematic regime relevant for this analysis, the π^0 transverse momenta are typically lower than those for ATLAS discussed in Section 4.3, leading to large opening angles between the decay photons. In addition the same case as before arrives there, the ΔR distribution between photons originating from the same parent pion are larger than the minimum resolution of the detector to distinguish them. Therefore, photon merging can be safely neglected, similarly to previous phase-space studies for the ATLAS phase space analysis and therefore one should expect to nearly always see 4 photons in the final state (if all of them are in the acceptance of the detector).
There are many possible combinations to form a two-photon final state from the four photons produced in the $\gamma\gamma \to \pi^0\pi^0 \to (\gamma\gamma)(\gamma\gamma)$ process. However, photon pairs originating from the same parent pion yield a narrow invariant mass peak around the π^0 mass and can therefore be efficiently rejected; therefore, they do not contribute to the background. Since the generated MC sample is produced with a pion transverse momentum requirement of $p_{\mathrm{T}}^{\pi^0} > 0.3$ GeV applied to pions, not photons - the resulting p_{T} distribution of the final-state photons is expected to be softer, as also observed in the ATLAS phase space analysis. In the present case, different calorimeters have different transverse momentum thresholds, which further complicates the analysis. To estimate the potential background contribution from the dipion process, diphoton final state mimicking the signal is constructed by randomly pairing one photon from each decaying pion and checking whether the resulting photon pair satisfies the acceptance criteria, using the widest transverse momentum threshold of $p_{\mathrm{T}} > 0.3$ GeV. Photon pairs composed in this way, from photons belonging to different pions, represent the dominant and irreducible background topology for the $\gamma\gamma \to \gamma\gamma$ analysis for the ALICE phase space. Therefore calculated MC cross section for such topology of this process is: 25321.54 nb and 488.83 nb for central Barrel and forward FoCal region respectively.
In Figure 6.5, the invariant mass distributions of the diphoton system are shown for both the signal ($\gamma\gamma \to \gamma\gamma$) and the dominant background originating from $\gamma\gamma \to \pi^0\pi^0$ events for central and forward regions. As one can see, the background contribution is very large, especially at lower invariant masses which is the region of primary interest for the ALICE measurement. Efficiencies marked on the histograms as ε will be defined later in the text as

6.1. Exact numbers are reported in Tables 6.5 and 6.6 for the central and forward regions, respectively.

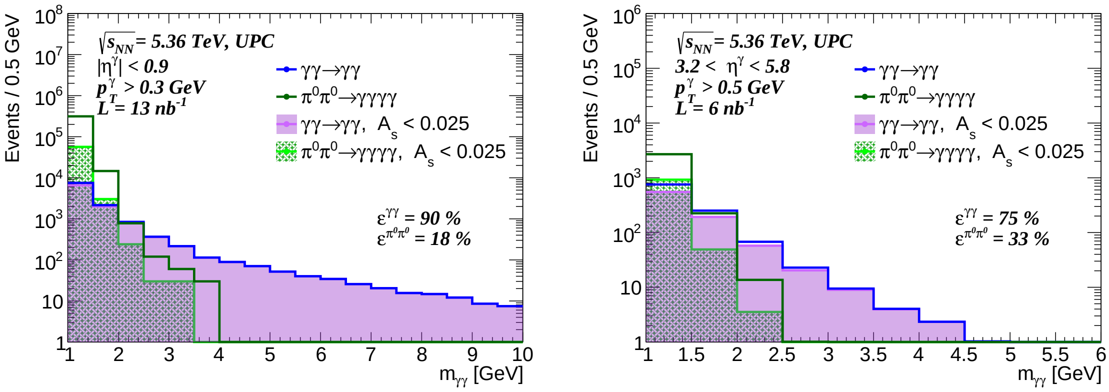

Figure 6.5: Expected yields of LbyL scattering and $\gamma\gamma \to \pi^0\pi^0$ background in the ALICE detector in the central (left) and forward (right) regions for $\mathcal{L} = 13$ nb^{-1} and $\mathcal{L} = 6$ nb^{-1}, respectively as a function of the diphoton invariant mass coming from the UPCGEN MC generator. The same distributions after applying a scalar asymmetry cut of $A_S < 0.025$ are overlaid for comparison.

Fortunately, although the background is numerically dominant compared to the signal, it exhibits a distinct shape in the invariant mass distribution. The background decreases rapidly with increasing mass, becoming practically negligible above 4 GeV in the barrel region and above 2.5 GeV in FoCal. Nevertheless, measurements at lower masses than these thresholds are also of interest. It is feasible to extend the analysis down to approximately 2.5 GeV in the barrel and 2 GeV in FoCal, where the background is still lower than the signal (see logarithmic scale). Below these values, however, the background begins to approach the signal level, and at even lower masses it becomes substantially larger. A possible solution is to define an appropriate signal region by applying a cut on a suitable kinematic variable. Scalar asymmetry (4.3) can be used in this case as defined in Section 4.1. This variable provides sensitivity to the event topology and can be used to optimize the selection of signal events. To determine an optimal cut value on A_S, the selection efficiency is defined as the ratio of the number of events after applying the A_S cut to the number of events before the cut:

$$\varepsilon(A_S) = \frac{N^{\text{after}}}{N^{\text{before}}} \tag{6.1}$$

The distributions of obtained selection efficiencies for signal and background processes are shown in Figure 6.6. In addition 2d histograms of invariant mass vs scalar asymmetry A_S are analysed to evaluate the dependence of the remaining number of events on the chosen cut. In Figure 6.7 A_S vs $m_{\gamma\gamma}$ 2d distribution is shown for the forward region phase space of FoCal. Same histogram but for the central phase space is shown in appendix A.4, results there are similar. Differences between the barrel and FoCal regions are apparent; in the forward region, the background distribution overlaps with a larger fraction of the signal than in the central region. Applying a cut of $A_S < 0.025$ retains more than 90% of the signal, while the background is reduced by approximately four-fifths (leaving only 18%) in the barrel region, and similarly 75% of the signal and 33% of the background remain in FoCal. This behaviour reflects the degree of overlap between signal and background observed in the previous figures.

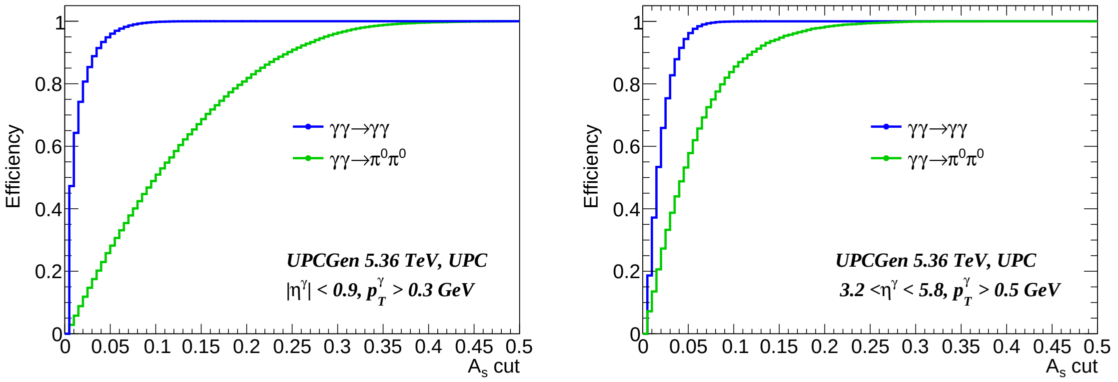

Figure 6.6: Expected LbyL scattering signal and the potential $\gamma\gamma \to \pi^0\pi^0$ background selection efficiencies, expressed as the number of events before and after applying a cut on the scalar asymmetry A_S.

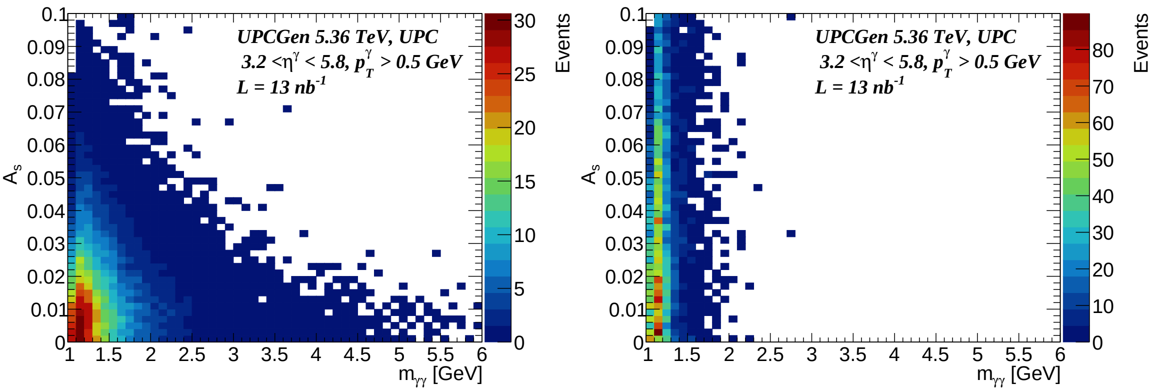

Figure 6.7: Expected LbyL scattering signal (left) and the potential $\gamma\gamma \to \pi^0\pi^0$ background (right) 2d color maps of acoplanarity A_S vs diphoton invariant mass $m_{\gamma\gamma}$ distributions for ALICE FoCal forward phase space coming from UPCGen MC generator.

Tables 6.5 and 6.6 summarize the selection efficiencies for several scalar asymmetry thresholds, illustrating the importance of choosing an optimal value. For a tighter cut of $A_S < 0.01$, the corresponding histograms are shown again (Figure 6.8), as this selection provides a clean signal in invariant mass down to the 3 GeV for the central and nearly clear on 2 GeV for the forward region. Additional histograms corresponding to other A_S cuts listed in the Tables are provided in Appendix (A.5).

Table 6.5: Signal (LbyL) and background ($\gamma\gamma \to \pi^0\pi^0$) yields and efficiencies in the barrel region for different scalar asymmetry (A_S) cuts.

Before cuts: $N_{sig}^{before} = 11593$, $N_{bkg}^{before} = 329180$				
A_S	N_{sig}^{after}	N_{bkg}^{after}	ε_{sig} [%]	ε_{bkg} [%]
0.025	10455	59936	90.2	18.2
0.020	9970	50211	86.0	15.3
0.017	9593	42558	82.7	12.9
0.010	8133	24280	70.2	7.4
0.005	6061	13146	52.3	4.0

Table 6.6: Signal (LbyL) and background ($\gamma\gamma \to \pi^0\pi^0$) yields and efficiencies in the focal region for different scalar asymmetry (A_S) cuts.

Before cuts: $N_{sig}^{before} = 1115$, $N_{bkg}^{before} = 2934$				
A_S	N_{sig}^{after}	N_{bkg}^{after}	ε_{sig} [%]	ε_{bkg} [%]
0.025	840	976	75.3	33.3
0.020	734	800	65.8	27.3
0.017	654	685	58.6	23.3
0.010	414	397	37.1	13.5
0.005	208	211	18.6	7.2

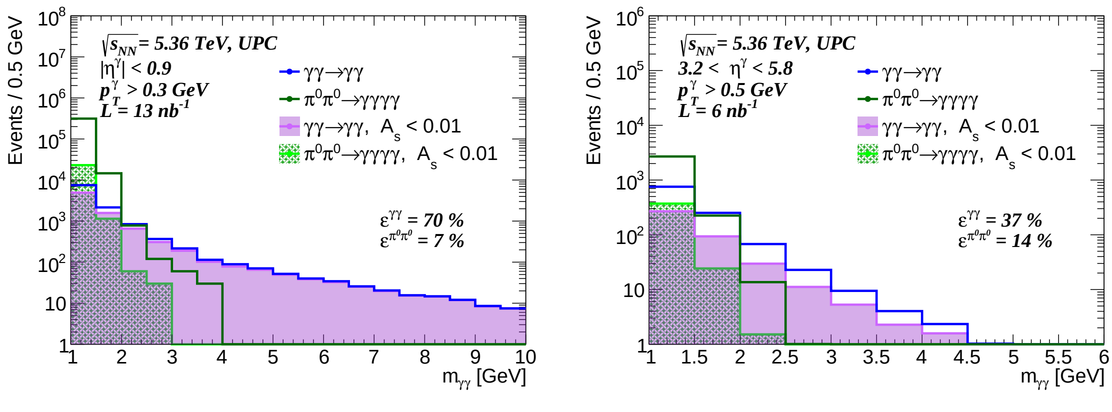

Figure 6.8: Expected LbyL scattering and potential $\gamma\gamma \to \pi^0\pi^0$ background yields in the ALICE detector in the central (left) and forward (right) regions for $\mathcal{L} = 13$ nb^{-1} and $\mathcal{L} = 6$ nb^{-1}, respectively as a function of the diphoton invariant mass coming from the UPCGEN MC generator. The same distributions after applying a scalar asymmetry cut of $A_S < 0.01$ are overlaid for comparison.

6.3.2 Dielectron production

The exclusive dielectron production process ($\gamma\gamma \to e^+e^-$) can also constitute a potential background to the LbyL scattering signal in the ALICE phase space, similarly to the case of the ATLAS experiment. It will contribute as background if neither electron track is reconstructed or if both electrons undergo hard bremsstrahlung emitting high-energetic photons. This process was simulated using the SuperChic 5.3 (5.6) MC generator for the forward (central) regions, applying fiducial requirements corresponding to the barrel and FoCal phase spaces in Pb-Pb UPCs at $\sqrt{s_{\mathrm{NN}}} = 5.36$ TeV. Selection criteria are $p_{\mathrm{T}}^{e} > 0.3$ GeV and $|\eta^e| < 0.9$ for the central region, and $p_{\mathrm{T}}^{e} > 0.5$ GeV, $3.2 < \eta^e < 5.8$ for the FoCal region. The obtained MC cross sections are 1172 ± 1.32 μb for the forward region and 12672.98 ± 13.92 μb for the central region, based on samples of 9000 and 20000 generated events, respectively. The relatively small size of the simulated samples is due to the long computation time required to generate this process with the SuperChic generator.
The obtained cross sections are several orders of magnitude higher than those of the LbyL signal process. In addition, SuperChic predicts that the shapes of the invariant mass distributions are nearly identical to those of LbyL, provided that no cuts are applied in either of the considered phase space regions. Due to its relatively high rate, the exclusive production of electron pairs can constitute a source of fake diphoton events. Furthermore, the kinematic distributions of these events, such as the diphoton acoplanarity, closely resemble those of the LbyL signal. This justifies the difficulty in distinguishing between the two processes without employing the tracking detector for a veto on tracks (to ensure no charged particles are associated with the energy clusters). Figure 6.9 shows the invariant mass distributions of both the LbyL signal process and the dielectron background ($\gamma\gamma \to e^+e^-$) on the same plot for both considered phase space regions.

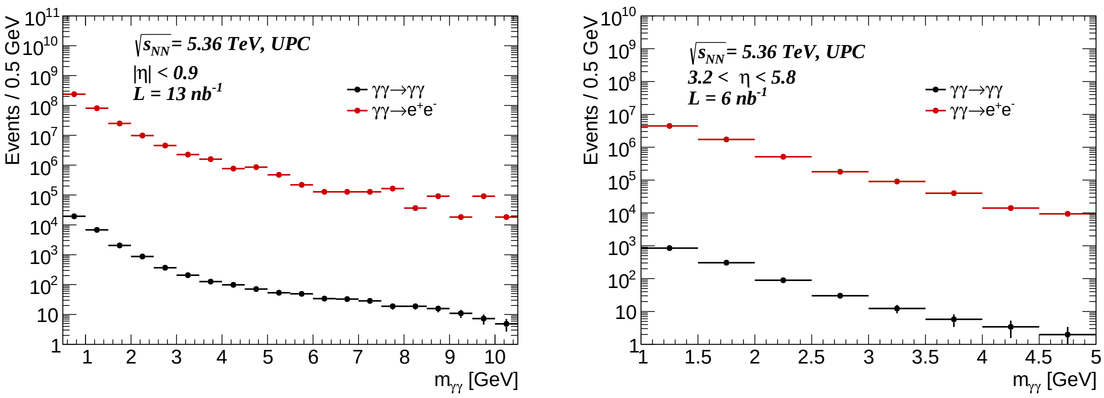

Figure 6.9: Expected LbyL scattering and potential $\gamma\gamma \to e^+e^-$ background yields in the ALICE detector in the central (left) and forward (right) regions for $\mathcal{L} = 13$ nb^{-1} and $\mathcal{L} = 6$ nb^{-1}, respectively as a function of the diphoton invariant mass coming from the SuperChic MC generator.

These distributions present truth-level information for all dielectron events. However, the background under consideration would only contribute if electrons from these events are not reconstructed as charged particles and are instead misidentified as photons, thereby mimicking the light-by-light (LbyL) scattering signal. An accurate estimate of this background therefore requires a full detector simulation, as truth-level information alone provides only an approximate production cross section of the underlying process. Following detector simulation, these distributions can change significantly due to reconstruction effects, acceptance losses, and particle misidentification.

In the ALICE experiment, charged-particle reconstruction in the central barrel is primarily performed using the Inner Tracking System (ITS) and the Time Projection Chamber (TPC), which provide high tracking efficiency for transverse momenta above $p_{\mathrm{T}} \approx 0.3$ GeV [32, 33]. Performance studies show that for primary electrons with $p_{\mathrm{T}} > 0.3$ GeV, the combined ITS, TPC tracking efficiency exceeds 90% in pp and peripheral heavy-ion collisions, and remains above approximately 85% even in high-multiplicity Pb-Pb events. Consequently, the probability for a single electron to remain unreconstructed in this kinematic region is at most of order $\mathcal{O}(10\%)$.
Assuming independent reconstruction probabilities for the two charged particles, the probability that both electrons from a $\gamma\gamma \to e^+e^-$ process are not reconstructed as tracks can be approximated as:

$$P_{\mathrm{miss}}^{(2)} \simeq (1 - \varepsilon_{\mathrm{track}})^2, \tag{6.2}$$

where $\varepsilon_{\mathrm{track}}$ denotes the single-particle tracking efficiency. For $\varepsilon_{\mathrm{track}} = 0.9$ (0.95), this results in $P_{\mathrm{miss}}^{(2)} \approx 1\times10^{-2}$ (2.5×10^{-3}), demonstrating a strong suppression of the dielectron background already at the tracking level.
Furthermore, only a subset of these unreconstructed electrons can mimic photons in the calorimeter. Electron misidentification as photons is primarily driven by hard bremsstrahlung occurring in the detector material upstream of the calorimeter, which can lead to electromagnetic showers with little or no associated track information. The probability of such processes depends sensitively on the material budget traversed by the electrons prior to reaching the calorimeter surface, and therefore on the detailed geometry of the ALICE sub-detectors and the future FoCal system.
The probability of electron misidentification in the barrel region may be enhanced due to the lower transverse momentum threshold of 0.3 GeV, compared to 0.5 GeV in the FoCal region, as reconstruction efficiency typically decreases at lower energies. Overall, this effect depends on the specific design of ALICE sub-detectors and the future FoCal calorimeter. Moreover, the probability of hard bremsstrahlung, which is a key factor in electrons mimicking photons, depends strongly on the material encountered by the electrons before reaching the calorimeter surface. Therefore, these background predictions require further investigation using detector simulations, alongside a $\gamma\gamma \to e^+e^-$ selection based on reconstructed tracks and other kinematic, detector-dependent variables as, for example in Section 5 of this thesis.

7. Summary

In this thesis, the role of MC generators for ultra-peripheral collisions of lead ions at the LHC has been demonstrated, and an analysis of real UPC data from 2025 has been performed.

For the ATLAS experiment, several rare processes with two photons in the final state were investigated. First, using the SuperChic and UPCgen MC generators, LbyL scattering was studied at the centre-of-mass energy of $\sqrt{s_{\mathrm{NN}}} = 5.36$ TeV, corresponding to the Run-3 (2023-2026) conditions at the LHC. This analysis demonstrated the basic properties of the process, including the shapes of various kinematic distributions, such as diphoton acoplanarity as well as more exotic observables like scalar and vector asymmetries. The obtained MC cross section is 132.46 ± 0.54 nb within the ATLAS fiducial acceptance, requiring photons with transverse momentum $p_{\mathrm{T}} > 2$ GeV, pseudorapidity $|\eta| < 2.4$ and diphoton invariant mass $m_{\gamma\gamma} > 4$ GeV. The dependence of the process on the collision energy $\sqrt{s_{\mathrm{NN}}}$ was also examined; no significant differences in the shapes of the distributions were observed. In addition, different ion-breakup topologies were investigated in more detail for LbyL scattering within the MC production showing a dependence of energy-related observables. The ratio of events in which both nuclei remain intact ($0n0n$) to the inclusive ($AnAn$) category is $f_{0n0n} = 78.63 \pm 0.05$ % for the ATLAS fiducial region which is consistent with [20].
Besides the LbyL signal process, several background processes were analysed at the generator level. The CEP ($gg \to \gamma\gamma$) process was studied using SuperChic MC generator, including an evaluation of the uncertainties related to PDFs. For the first time, a detailed study was performed of dipion production ($\gamma\gamma \to \pi^0\pi^0$) using the UPCgen MC generator. This leads to the conclusion that within the current ATLAS fiducial requirements, this background can be safely neglected. In addition, the rare $\gamma\gamma \to e^+e^-\gamma\gamma$ process was simulated using the MadGraph5 MC generator, also showing a negligible contribution to the LbyL signal region.

An analysis of real UPC data collected by ATLAS was also performed, as the result of the internship at CERN by Author who assisted in heavy-ion data taking in November 2025. The efficiency of the vpix60 selection at HLT was evaluated for the 2025 UPC Pb-Pb data using the $\gamma\gamma \to e^+e^-$ process selection. The trigger efficiency was found to be high, approaching unity as a function of the dielectron rapidity y_{ee}. However, an issue of the additional background present in the detector was observed, which will require further investigation in future analyses based on the 2025 UPC data.

Finally, feasibility studies for the ALICE detector phase space were carried out, providing motivation for a future LbyL scattering analysis in this experiment for the first time. The ALICE fiducial acceptance, defined by $|\eta| < 0.9$ allows studies down to diphoton invariant masses of the order of $m_{\gamma\gamma} \sim \mathcal{O}(1 \text{ GeV})$ in contrast to the higher mass threshold imposed by the ATLAS reconstruction requirements. Signal predictions, together with the two main potential background processes were discussed for the low invariant mass region. The predicted signal yield is of the order of 2300 for the assumed integrated luminosity. The studied backgrounds (dipion and dielectron production) are under control, making measurements at slightly higher invariant masses than the lowest region of interest feasible, with a non-negligible expected event yield, and thus enabling a potential first LbyL scattering analysis in the ALICE experiment.

Bibliography

[1] C. F. von Weizsäcker. "Radiation emitted in collisions of very fast electrons". In: *Zeitschrift für Physik* 88 (1934). DOI: 10.1007/BF01333110.

[2] H. Euler and W. Heisenberg. "Consequences of Dirac's theory of positrons". In: *Zeitschrift für Physik* 98 (1936). DOI: 10.1007/BF01343663.

[3] F. Halzen and A. D. Martin. *Quarks and Leptons: An Introductory Course in Modern Particle Physics*. Wiley, 1984.

[4] ATLAS Collaboration. "Evidence for light-by-light scattering in heavy-ion collisions with the ATLAS detector at the LHC". In: *Nature Physics* 13 (2017). DOI: 10.1038/nphys4208.

[5] CMS Collaboration. "Evidence for light-by-light scattering and searches for axion-like particles in ultraperipheral PbPb collisions at $\sqrt{s_{NN}}$=5.02 TeV". In: *Physics Letters B* 797 (2019), p. 134826. DOI: https://doi.org/10.1016/j.physletb.2019.134826.

[6] ATLAS Collaboration. "Measurement of light-by-light scattering and search for axion-like particles with 2.2 nb-1 of Pb+Pb data with the ATLAS detector". In: *Journal of High Energy Physics* 2021.3 (Mar. 2021). DOI: 10.1007/jhep03(2021)243.

[7] ATLAS Collaboration. "Search for new phenomena in events with at least three photons collected in pp collisions at $\sqrt{s} = 8$ TeV with the ATLAS detector". In: *The European Physical Journal C* 76.4 (Apr. 2016). DOI: 10.1140/epjc/s10052-016-4034-8.

[8] ATLAS Collaboration. "Search for pairs of highly collimated photon-jets in pp collisions at $\sqrt{s} = 13$ TeV with the ATLAS detector". In: *Phys. Rev. D* 99 (1 Jan. 2019), p. 012008. DOI: 10.1103/PhysRevD.99.012008.

[9] M.G. Albrow, T.D. Coughlin, and J.R. Forshaw. "Central exclusive particle production at high energy hadron colliders". In: *Progress in Particle and Nuclear Physics* 65.2 (Oct. 2010), pp. 149–184. DOI: 10.1016/j.ppnp.2010.06.001.

[10] M. Kłusek-Gawenda and A. Szczurek. "Exclusive production of large invariant mass pion pairs in ultraperipheral ultrarelativistic heavy ion collisions". In: *Physics Letters B* 700.5 (June 2011), pp. 322–330. DOI: 10.1016/j.physletb.2011.05.015.

[11] M. Tanabashi et al. "Review of Particle Physics". In: *Phys. Rev. D* 98 (3 Aug. 2018), p. 030001. DOI: 10.1103/PhysRevD.98.030001.

[12] N. Metropolis. "The Beginning of the Monte Carlo Method". In: *Los Alamos Science*. 1987, pp. 125–130.

[13] Mark Thomson. *Modern Particle Physics*. 2nd. Cambridge University Press, 2013.

[14] Bo Andersson et al. "Parton Fragmentation and String Dynamics". In: *Phys. Rept.* 97 (1983), pp. 31–145. DOI: 10.1016/0370-1573(83)90080-7.

[15] S. Agostinelli et al. "Geant4-a simulation toolkit". In: *Nucl. Instrum. Meth. A* 506.3 (2003), pp. 250–303. DOI: https://doi.org/10.1016/S0168-9002(03)01368-8.

[16] L. A. Harland-Lang, V. A. Khoze, and M. G. Ryskin. "Exclusive physics at the LHC with SuperChic". In: *Eur. Phys. J. C* 79 (2019). DOI: 10.1140/epjc/s10052-018-5772-6.

[17] Nazar Burmasov et al. "Upcgen: A Monte Carlo simulation program for dilepton pair production in ultra-peripheral collisions of heavy ions". In: *Computer Physics Communications* 277 (2022), p. 108388. DOI: https://doi.org/10.1016/j.cpc.2022.108388.

[18] The ATLAS Collaboration. "The ATLAS Experiment at the CERN Large Hadron Collider". In: *Journal of Instrumentation* 3.08 (Aug. 2008), S08003. DOI: 10.1088/1748-0221/3/08/S08003.

[19] Mariola Kłusek-Gawenda et al. "Light-by-light scattering in ultraperipheral heavy-ion collisions at low diphoton masses". In: *Phys. Rev. D* 99 (9 May 2019), p. 093013. DOI: 10.1103/PhysRevD.99.093013.

[20] P. Jucha, M. Kłusek-Gawenda, and A. Szczurek. "Neutron emission associated with $\gamma\gamma \rightarrow \gamma\gamma$ scattering in ultraperipheral collisions of heavy ions at the LHC". In: *Phys. Rev. D* (2025). DOI: 10.1103/qf5z-wsmb.

[21] G Baur. "Coherent $\gamma\gamma$ and γA interactions in very peripheral collisions at relativistic ion colliders". In: *Physics Reports* 364.5 (July 2002), pp. 359–450. DOI: 10.1016/s0370-1573(01)00101-6.

[22] Jon Butterworth et al. "PDF4LHC recommendations for LHC Run II". In: *Journal of Physics G: Nuclear and Particle Physics* 43.2 (Jan. 2016), p. 023001. DOI: 10.1088/0954-3899/43/2/023001.

[23] David d'Enterria and Gustavo G. da Silveira. "Observing Light-by-Light Scattering at the Large Hadron Collider". In: *Physical Review Letters* 111.8 (Aug. 2013). DOI: 10.1103/physrevlett.111.080405.

[24] Spencer R. Klein et al. "STARlight: A Monte Carlo simulation program for ultra-peripheral collisions of relativistic ions". In: *Computer Physics Communications* 212 (Mar. 2017), pp. 258–268. ISSN: 0010-4655. DOI: 10.1016/j.cpc.2016.10.016.

[25] ATLAS Collaboration. "Exclusive dielectron production in ultraperipheral Pb+Pb collisions at $\sqrt{s_{\mathrm{NN}}} = 5.02$ TeV with ATLAS". In: *Journal of High Energy Physics* 2023.6 (June 2023). ISSN: 1029-8479. DOI: 10.1007/jhep06(2023)182.

[26] ATLAS Collaboration. *ANA-HION-2023-10-INT1*. CERN internal note. Available via CERN Document Server (CDS). 2025.

[27] K. Zając and A. Matyja. "Feasibility Studies of Light-by-light Scattering in ALICE with FoCal Phase Space". In: *Acta Physica Polonica B Proceedings Supplement* 18, 5-A36 (June 2025). DOI: 10.5506/APhysPolBSupp.18.5-A36.

[28] ALICE Collaboration. "Performance of the ALICE experiment at the CERN LHC". In: *International Journal of Modern Physics A* 29.24 (Sept. 2014), p. 1430044. ISSN: 1793-656X. DOI: 10.1142/s0217751x14300440.

[29] S. Acharya et al. In: *Journal of Instrumentation* 18 (2023), P08007. DOI: 10.1088/1748-0221/18/08/P08007.

[30] S. Acharya et al. In: *Journal of Instrumentation* 14 (2019), P05025. DOI: 10.1088/1748-0221/14/05/P05025.

[31] ALICE Collaboration. *Technical Design Report of the ALICE Forward Calorimeter (FoCal)*. Tech. rep. CERN-LHCC-2024-004; ALICE-TDR-022. Submitted by C. Loizides and W. Riegler. CERN, 2024. URL: https://cds.cern.ch/record/2890281/files/ALICE-TDR-022.pdf?version=5.

[32] ALICE Collaboration. “Event-by-event mean $p_{\mathbf{T}}$ fluctuations in pp and Pb–Pb collisions at the LHC”. In: *The European Physical Journal C* 74.10 (Oct. 2014). ISSN: 1434-6052. DOI: 10.1140/epjc/s10052-014-3077-y.

[33] ALICE Collaboration. “The ALICE experiment at the CERN LHC”. In: *Journal of Instrumentation* 3 (2008), S08002. DOI: 10.1088/1748-0221/3/08/S08002.

A. Appendix

This appendix presents additional Figures referenced in this thesis, provided to support the analysis without interrupting the main text.

A.1 Light-by-light scattering in ATLAS

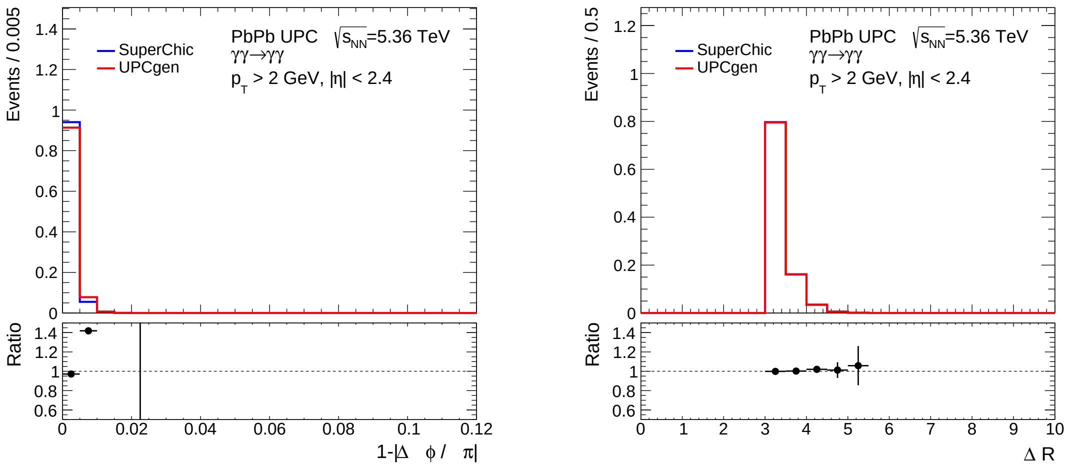

Figure A.1: Diphoton acoplanarity Aco (left) and ΔR (right) normalized distributions of final state photons from LbyL scattering ($\gamma\gamma \to \gamma\gamma$) coming from SuperChic 4.2 and UPCgen MC generators.

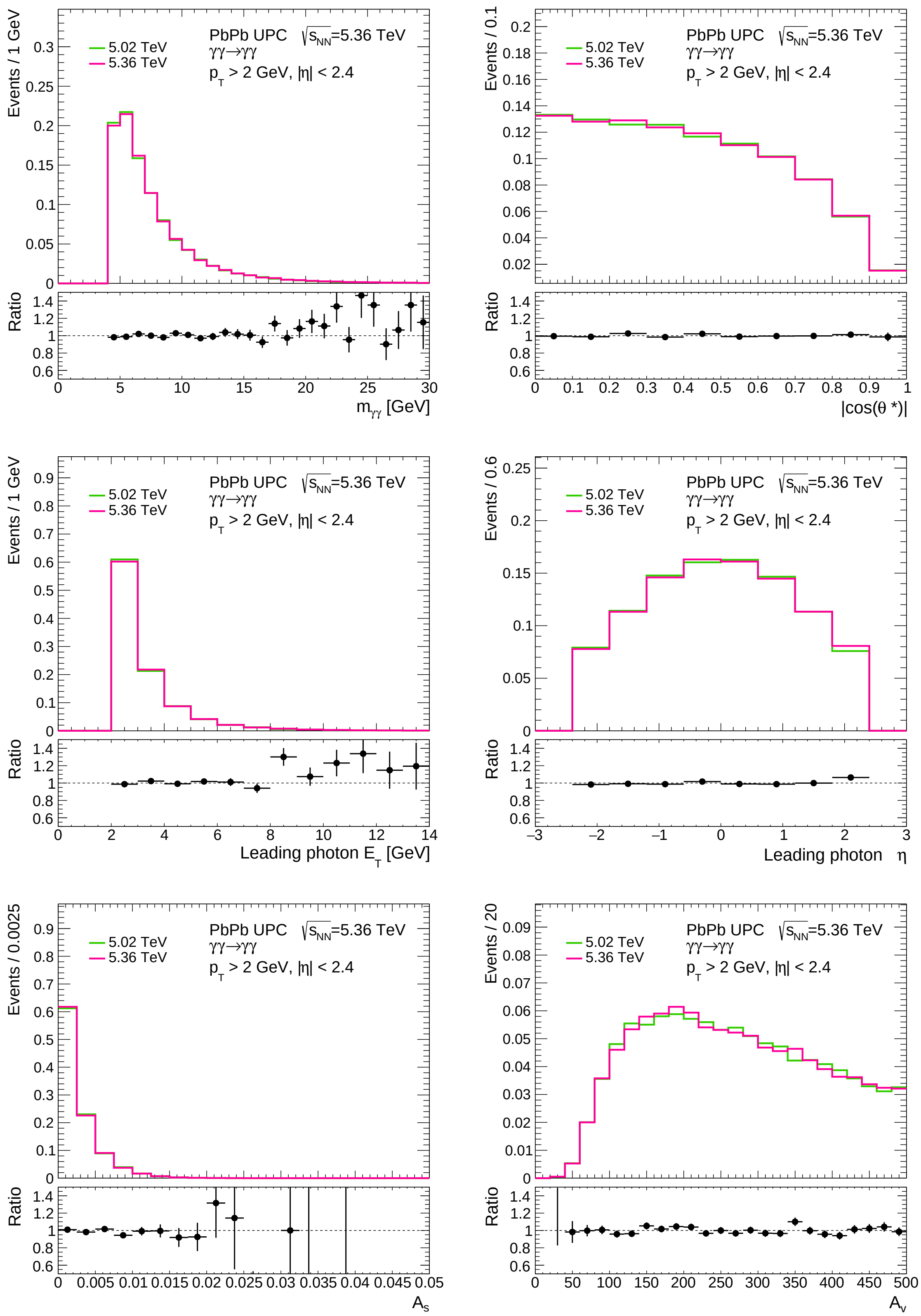

Figure A.2: Comparison of diphoton and photon observables obtained for $\sqrt{s_{\mathrm{NN}}} = 5.02$ and 5.36 TeV using SuperChic 4.2. Top to bottom: $m_{\gamma\gamma}$, $|\cos(\theta^{*})|$, leading photon p_{T} and η, A_{S}, and A_{v}.

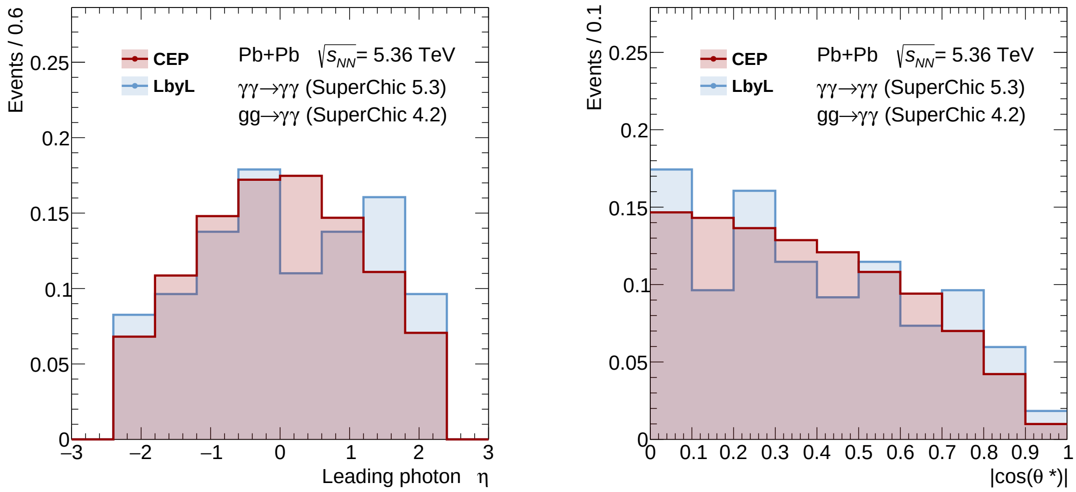

Figure A.3: Comparison of leading photon η (left) and $\cos(\theta^*)$ (right) shape distributions from LbyL scattering ($\gamma\gamma \rightarrow \gamma\gamma$) with incoherent CEP $gg \rightarrow \gamma\gamma$ process in the control region. Fluctuations visible for LbyL due to small number of events which fulfill Aco > 0.01 control region requirement.

A.2 Theoretical predictions for ALICE detector's phase space

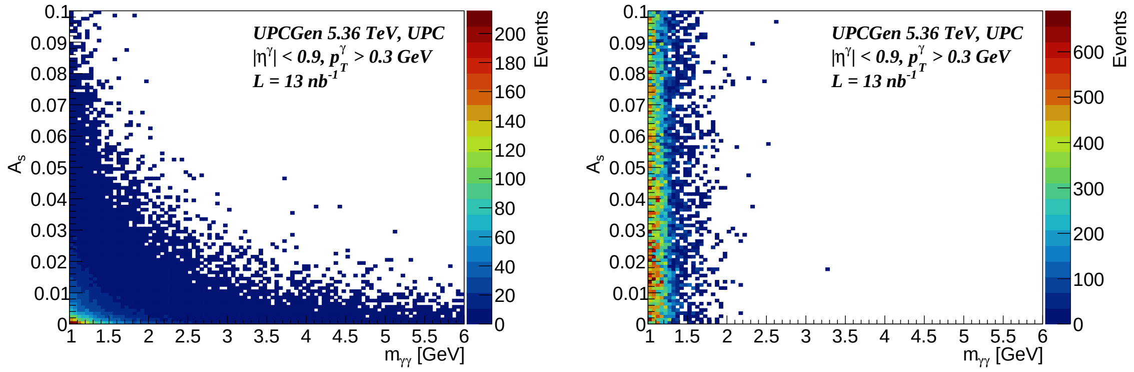

Figure A.4: Expected LbyL scattering signal (left) and the potential $\gamma\gamma \rightarrow \pi^0\pi^0$ background (right) 2d color maps of acoplanarity A_S vs diphoton invariant mass $m_{\gamma\gamma}$ distributions for ALICE barrel central phase space coming from UPCGen MC generator.

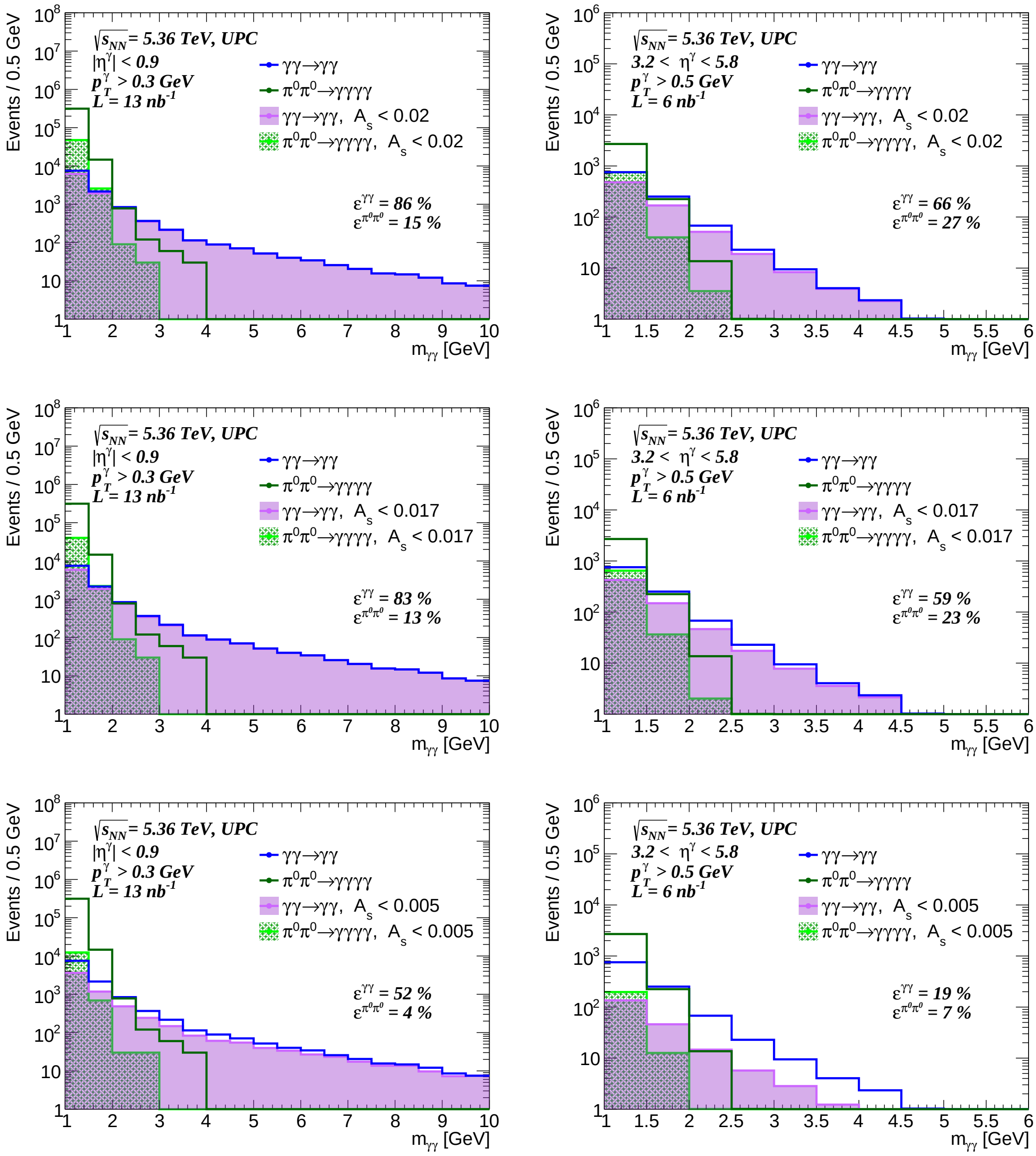

Figure A.5: Expected yields of LbyL scattering and $\gamma\gamma \to \pi^0\pi^0$ background in the ALICE detector in the central (left) and forward (right) regions for $\mathcal{L} = 13$ nb^{-1} and $\mathcal{L} = 6$ nb^{-1}, respectively, as a function of the diphoton invariant mass from the UPCGEN MC generator. Overlaid distributions correspond to different scalar asymmetry cuts: $A_S < 0.02$, $A_S < 0.017$, and $A_S < 0.005$ (from top to bottom).